A two-reaction-zones moving-interface model for predicting Ca(OH)_2-carbonation in concrete

Zentrum für Technomathematik

Fachbereich 3 – Mathematik und Informatik

A Two-Reaction-Zones Moving-Interface Model for Predicting $Ca(OH)_2$ Carbonation in Concrete

Michael Böhm **Jörg Kropp**

Adrian Muntean

Report 03–04

Berichte aus der Technomathematik

Report 03–04 **April 2003**

A Two-Reaction-Zones Moving-Interface Model for Predicting $Ca(OH)_2$-Carbonation in Concrete

Michael Böhm * Jörg Kropp † Adrian Muntean ‡

Abstract: Corrosion of steel reinforcement in concrete is essentially controlled by the change of pH near the steel bars. One of the major contributions to a drop in pH is the carbonation of $Ca(OH)_2$ and of other substances near the bars caused by atmospheric CO_2 diffusing in the dry parts and reacting in the wet parts of the concrete pores. In this note we propose a prediction model for $Ca(OH)_2$-carbonation. The model is a system of coupled partial differential equations with a moving interface at the carbonation front. It is supplemented by appropriate boundary and interface conditions and allows the prediction of the position of the carbonation front as well as of the concentrations of CO_2, rest-$Ca(OH)_2$ and of $CaCO_3$. Special emphasis is laid on the discussion of the reaction near and remote from the carbonation-reaction front. The main tool is the introduction of two separate reaction regions. The formulation of the model allows for $1D$ to $3D$ concrete objects. Comparison with penetration curves based on accelerated carbonation experiments as well as with simulated curves show that the model is appropriate for a wide range of concretes.

Key words: Concrete corrosion modeling, carbonation, moving carbonation layer, two-reaction-zones model, coupled partial differential equations, moving-boundary problem.

Acknowledgments: This project has been supported by the German Science Foundation (DFG) by a grant through the Special-Focus program 'Vorhersage des zeitlichen Verlaufs von physikalisch-technischen Schädigungsprozessen an mineralischen Werkstoffen' (SPP 1122). The authors thank Prof. L. Franke (TU Hamburg-Harburg, Germany) for supplying us with experimental data from his accelerated carbonation experiments.

1 Introduction

One of the most appreciated features of reinforced concrete structures is their durability, which is endangered by the corrosion of the reinforcing steel. Initially the steel bars are covered by a thin oxide layer which is formed and maintained via its surface by a high alkaline neighbourhood with pH between 12 and 13. The major contributor to the high pH is $Ca(OH)_2$. Depassivation of the steel happens when Cl^- reaches the bars or if the amount of $Ca(OH)_2$ near the bars is reduced by reaction with CO_2 - the *carbonation*, leading to pH well below 9. At a very general level, the Cl^-- scenario is pre-dominant under marine

*ZeTeM, FB3(Mathematik), University of Bremen, Germany, e-mail: mbohm@math.uni-bremen.de
†Institut für Baustofftechnologie, Hochschule Bremen, Germany, e-mail: kropp@fbb.hs-bremen.de
‡ZeTeM, FB3(Mathematik), University of Bremen, Germany, e-mail: muntean@math.uni-bremen.de

conditions, whereas carbonation is dominant under atmospheric exposure and humidity between 0.4 and 0.7. Moreover, there is some interaction between the two mechanisms - with respect to chloride threshold levels and chloride ingress.

This note is a continuation of Ref. [9], in which the concept of a moving carbonation zone and a moving carbonation interface has been introduced and discussed. In the present note we introduce the concept of two reaction zones - one near or at the so-called carbonation front, the second one behind from the first, following the carbonation front.

The aim of this note is to show that this way of modeling captures the typical features of the $Ca(OH)_2$-carbonation process such as the experimentally verified reaction zone and the fact that after some initial carbonation (in a possibly very narrow reaction zone) the carbonation degree increases gradually until it reaches its maximum.

Experimental results of an accelerated carbonation experiment (*ace*) will be used for verification of the model.
The main results are summarized in section 5.5.

2 The two-reaction zones model. Introduction

2.1 Generalities

Experimental observation yields the following two typical phenomena during carbonation processes in concrete samples: The concrete sample, Ω, can roughly be divided in three regions - the uncarbonated part Ω_2, a partially carbonated part Ω_{12} and an (almost) completely carbonated part Ω_{11}. The first part is characterized by the complete lack of carbonated substances, the last part contains up to the maximally possible amount of carbonates and in the middle part the concentration of carbonated substances might increase over time. The bulk of the initiating carbonation reaction seems to take place in a very narrow layer $\Omega_\varepsilon \subseteq \Omega_{12}$ adjacent to the uncarbonated part Ω_2. In most cases this initial reaction does not consume all carbonatable products due to the fact that there may not be a sufficient amount of CO_2 to carbonate everything or because some of the carbonatable products are initially encapsulated (which is just a synonym for not yet being available for reaction) and become available for carbonation only after some time. Fig. 1 depicts the geometry of the situation. Fig. 3 depicts possible choices for modeling areas Ω in the sample in Fig. 1.

Fig. 5 shows possible scenarios for the advancements of the carbonated zone, the reaction zone and the uncarbonated zone.

Note: In Fig. 5 proportions do not correspond to reality - which is more like

$$width \text{ of } \Omega_\epsilon(t) \ll width \text{ of } \Omega_1(t) \ll width \text{ of } \Omega(t).$$

In this note we choose the time scale such that $t = 0$ corresponds to some time $\tau_1 > \tau_0$ in Fig. 5, i.e. in the present situation there is initially a (possibly very small) carbonated part $\Omega_1(0)$. The reference figure, depicting the initial geometry, is Fig. 6.

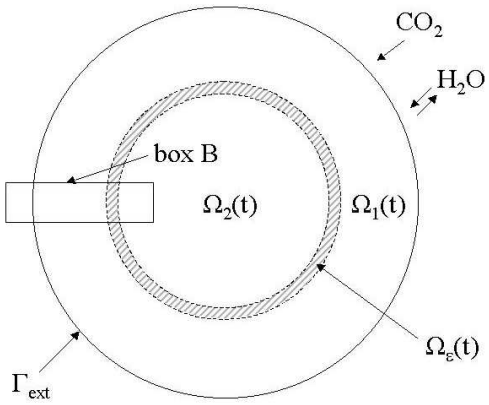

Figure 1: Cross section of a circular cylindrical concrete sample $\mathfrak{S}$ undergoing carbonation. Atmospheric CO_2 and water (humidity) enter $\mathfrak{S}$ and react with the carbonatable products in $\mathfrak{S}$. A relatively sharp reaction zone Ω_ϵ divides the uncarbonated part $\Omega_2(t)$ and the rest $\Omega_1(t)$ of $\mathfrak{S}$. Carbonation continues in $\Omega_\epsilon(t)$ and, to a lesser extent, in $\Omega_1(t)$. $\Gamma(t)$ is a curve in the center of Ω_ϵ which might serve as a substitute for the reaction zone Ω_ϵ (cf. Ref. [9]). All regions change with respect to time t. In particular $\Omega_1(t)$ grows and $\Gamma(t)$ moves inwards. The geometrical proportions are exaggerated.

2.2 Specifics

CO_2 enters Ω from the outside through the exterior bounadry Γ_{ext}, moves in the air-filled parts Ω_{pa} of the pores, enters the water-filled parts Ω_{pw} of the pores and reacts there with $Ca(OH)_2(aq)$. The reaction is simplified as

$$Ca(OH)_2 + CO_2 \overset{H_20}{\rightarrow} CaCO_3 + H_2O \tag{1}$$

and is modeled by *two* (possibly) different reaction rates - a volume rate η_{Rv}, concentrated on $\Omega_1(t)$, and (a possibly different) volume rate $\eta_{R\Gamma\epsilon}$ concentrated on $\Omega_\epsilon(t)$. No CO_2 enters the zone $\Omega_2(t)$ which is assumed to be untouched by CO_2. Some $Ca(OH)_2(aq)$ is initially present to establish a saturated pore solution. It is consumed by the reaction (1) and can be re-produced by dissolution or other mechanisms. Once $CaCO_3$ is produced by (1) it precipitates instantaneously - in particular it is assumed that there is no $CaCO_3(aq)$-flux. Water is initially present in entire concrete sample Ω. Its concentration is changed due to exterior in- or outflow through Γ_{ext} as well as by the reaction (1). Once CO_2 reaches the boundary Γ_r (cf. Fig. 2 (b)) of Ω_ϵ, it 'tries' to diffuse into $\Omega_1(t)$. Ultimately one can this consider as the cause of the forward motion of the reaction zone.

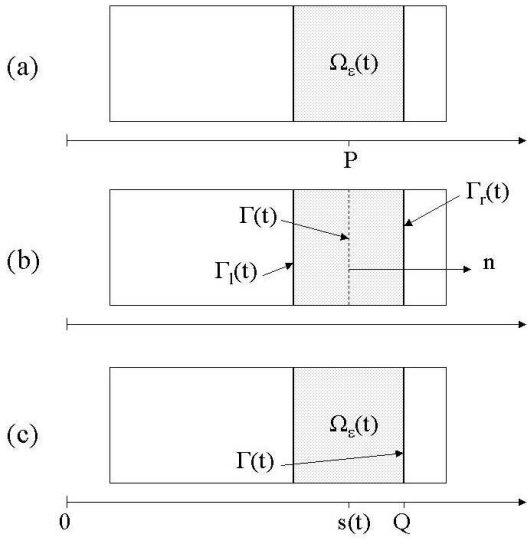

Figure 2: Disproportionally magnified box B from Fig. 1 with carbonation zone $\Omega_\epsilon(t)$ and two candidates for the definition of the 'carbonation front interface' $\Gamma(t)$ (center-lined surface or inner surface of $\Omega_\epsilon(t)$). (b) matters most here. The width of $\Omega_\epsilon(t)$ is ϵ.

2.3 Notations

$D_{\overline{w}k}$ - effective diffusion coefficient for moisture in $\Omega_k(t), k = 1, 2, \epsilon$
$D_{\overline{c}k}$ - effective diffusion coefficient for $CO_2(aq)$,
$D_{\overline{d}k}$ - effective diffusion coefficient for $CO_2(g)$,
$D_{\overline{h}k}$ - effective diffusion coefficient for $Ca(OH)_2(aq)$,
ϕ_k - volumetric porosities in $\Omega_k(t), k = 1, 2$, with $\phi_{ks} = 1 - \phi_k$,
ϕ_w, ϕ_a - water and air filled, respectively, fraction of the pores in $\Omega_1(t)$, $\phi_a + \phi_w = 1$,
$\eta_{R\Gamma}, \eta_{R\Gamma\varepsilon}$ - $\Gamma(t)$- and $\Omega_\varepsilon(t)$-concentrated surface- and volume-reaction rates for the reaction (1),
P_H - mass-transfer coefficient in Henry's law, Q_H - exchange factor in Henry's law,
$P_{\overline{h}kdiss}$ - factor in the dissolution law for $Ca(OH)_2$, $Q_{\overline{h}kdiss}$, $\overline{h}_{keq}$ - equilibrium concentration of $Ca(OH)_2, k = 1, 2, \epsilon$ (cf. 3.2.3),
$m^*_{Ca(OH)_2(s)}(x)$ - initial (i.e. before dissolution starts) concentration at x of $Ca(OH)_2(s)$ which is *available* for dissolution,
$S_{\overline{h}kdiss}$ - switching factor in the dissolution law,
κ, κ_1 - rate constants arising in Arrhenius' law.

3 The Model. Balance equations, interface, boundary and initial conditions

3.1 Balance equations in $\Omega_k(t), k = 1, \varepsilon, 2$

The geometrical situation is depicted in Fig. 3, Fig. 4 and in Fig. 6. Formally, we attribute to each region $\Omega_k(t), k = 1, \epsilon, 2$, individual source and sink terms (by reaction, dissolution, precipitation and by exchange between wet and dry parts of the pores). These individual

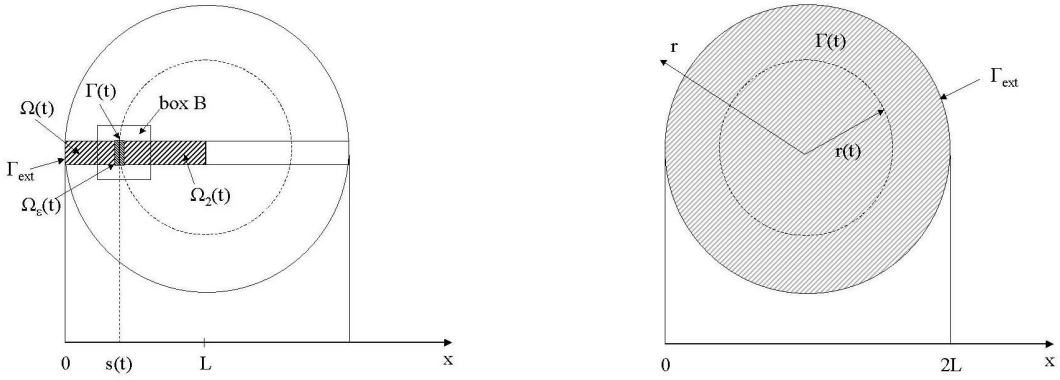

Figure 3: On the left: Fig. 3a, on the right Fig. 3b. Cross sections of concrete samples. The modeling area Ω is a rectangle or an interval, respectively. Interactions with the parts on top and below the bottom of Ω are neglected, vertical changes are considered as constant. The whole setting is $1D$. On the right: The whole cross section of the sample is the modeling area Ω, i.e. the setting is $2D$.

terms will be specified in section 3.2.

- Transport of CO_2 in the air phase of $\Omega_1(t) \cup \Omega_\varepsilon(t)$

$$\frac{\partial \overline{d}}{\partial t} + div(j_{\overline{d}}) = f_{\overline{d}Henry} \text{ in } \Omega_1(t) \cup \Omega_\epsilon(t). \tag{2}$$

- Transport and reaction of CO_2 in the wet phase of $\Omega_1(t) \cup \Omega_\varepsilon(t)$

$$\frac{\partial \overline{c}}{\partial t} + \underbrace{div(j_{\overline{c}})}_{\text{small!}} = f_{\overline{c}Henry} + f_{\overline{c}reac} \text{ in } \Omega_1(t) \cup \Omega_\epsilon(t). \tag{3}$$

- Transport, reaction and dissolution of $Ca(OH)_2$ in the wet phase of Ω

$$\frac{\partial \overline{h}}{\partial t} + div(j_{\overline{h}}) = f_{\overline{h}diss} + \underbrace{f_{\overline{h}reac}}_{\text{concentrated on} \Omega_1(t) \cup \Omega_\epsilon(t)} \text{ in } \Omega. \tag{4}$$

- Transport, reaction, loss by precipitation of $CaCO_3$ in the wet phase of $\Omega_1(t) \cup \Omega_\epsilon(t)$

$$\frac{\partial \phi_{1w} \overline{b}_w}{\partial t} + \underbrace{div(j_{\overline{b}_w})}_{=0} = f_{\overline{b}_w prec} + f_{\overline{b}_w reac} \text{ on } \Omega_1(t) \cup \Omega_\epsilon(t). \tag{5}$$

- The precipitated amount of $CaCO_3$ in $\Omega_1(t) \cup \Omega_\epsilon(t)$ is obtained from

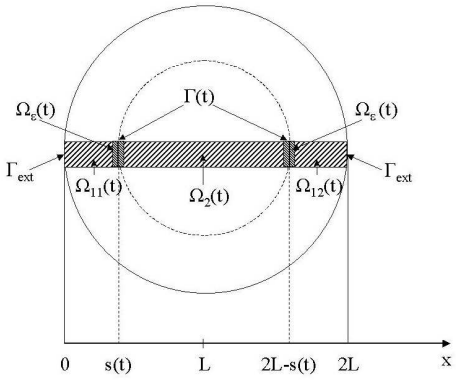

Figure 4: Another way of choosing the modeling area Ω for the cross section of a cylindrical domain. **Geometry of the carbonation process**: $\Omega :=$ reference modeling area section (Compare with Fig. 3). $\Omega_2 :=$ uncarbonated part, $\Omega_\epsilon :=$ carbonation-reaction zone adjacent to Ω_1, $\Gamma :=$ middle line (or middle surface) of $\Omega_\varepsilon, \Gamma_r$ and Γ_l - right and left boundary of Ω_ϵ, Ω_{11} and Ω_{12} are completely carbonated part and not yet completely carbonated part, $\Omega_1 := \Omega_{11} \cup \Omega_{12}$. All regions, except Ω, are time-dependent.

$$\frac{\partial \phi_{1s} \bar{b}_s}{\partial t} + \underbrace{div(j_{\bar{b}_s})}_{=0} = f_{\bar{b}_s prec} \text{ in } \Omega_1(t) \cup \Omega_\epsilon(t). \tag{6}$$

- The total $CaCO_3$-content in $\Omega_1(t) \cup \Omega_\epsilon(t)$ follows from

$$\frac{\partial \bar{b}}{\partial t} = f_{\bar{b} reac} \text{ in } \Omega_1(t) \cup \Omega_\varepsilon(t). \tag{7}$$

- Transport and generation of H_2O in Ω

$$\frac{\partial \overline{w}}{\partial t} + div(j_{\overline{w}}) = \underbrace{f_{\overline{w} reac}}_{\text{concentrated on } \Omega_1(t) \cup \Omega_\varepsilon(t)} \quad \text{in } \Omega. \tag{8}$$

3.2 Specification of reaction, exchange between dry and wet parts of the pores, dissolution and precipitation

3.2.1 Reaction rates

The major purpose of this note is to study the influence of variations of the reaction-rate *setting* for reaction (1) with respect to the model output (cf. section 5.4). As shown in Ref. [9], the structure (not that much the size!) of the reaction rates influences the output in a significant way. The fact that there is a (possibly very narrow) reaction zone, Ω_ϵ, does not require two *different* reaction rates - one on Ω_ϵ, the other one on Ω_1. There is some

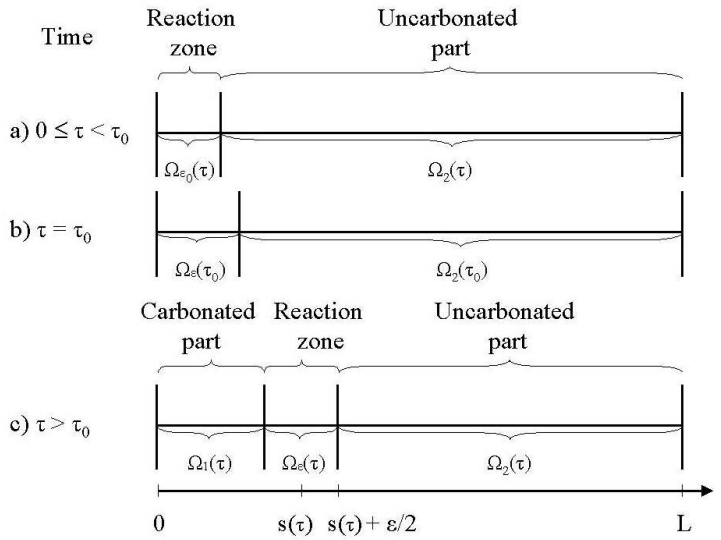

Figure 5: (a) Initially the reaction zone Ω_{ϵ_0} is in direct contact with the surface of the sample. (b) After some time τ_0 it reaches its maximal width ϵ. (c) Ω_ϵ advances into the uncarbonated zone Ω_2. Note: $\Gamma_{ext} \hat{=} x = 0$, $\Gamma_l \hat{=} s(\tau) - \frac{\epsilon}{2}$.

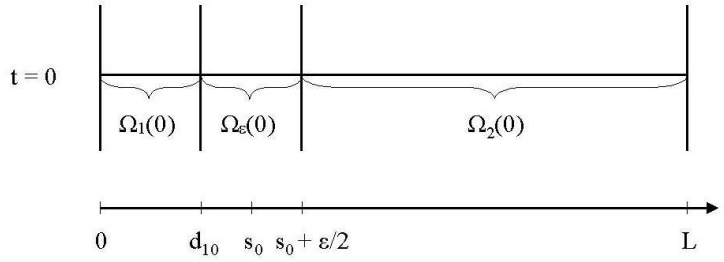

Figure 6: Specification of the initial layers. $\Omega_{\epsilon_0} := \Omega_\epsilon(0)$, $\Omega_{k0} := \Omega_k(0)$, $k = 1, 2$.

information available for the proper choice of a reaction rate - it is based on the analysis of carbonated samples. To our knowledge there is no such information available which refers exclusively to the carbonation-reaction zone Ω_ε. The common approach is to use *one* reaction rate for all of Ω_1 and Ω_ε. 'One' means in particular that all the constants entering the rate formula are the same on Ω_1 and Ω_ϵ, respectively. The tacit justification for this is that the reaction mechanism (expressed by the structure of the formula) is the same. Without that assumption one might be tempted to use different rates.

What is the 'right' reaction rate for (1)? Basically, besides doing something completely different, one has three options:
(a) Use reaction rates found by experiment;
(b) Use mass-action law type rates;
(c) Use variations of the mass-action law type rates.

We are not aware of a rich literature with respect to (a). Some authors use (b) - for academic purposes. There are (at least) two more or less common variations as in (c): One

modifies the mass action law by changing the exponents on the concentrations (cf. (12) below), another one (cf. (9)) tries to take the fact into account, that the humidity plays an important role on how fast reaction (1) happens. Using separate rates has its price: One needs more (experimental) a priori information to determine the corresponding constants. The gain is more flexibility, in particular when one deals with very narrow $\Omega_\epsilon(t)$ for which we are not aware of experimental data.

In this note we employ the following two reaction rates ((9) and (12)):

$$v\text{olume reaction rate for (1)} :=: \eta_{Rv} = \alpha A \exp(-\frac{E_0}{RT}) f_1 f_2 f_3 f_4 \quad (\text{on } \Omega_1(t)), \tag{9}$$

(cf. Refs. [41, 21] also cf. Ref. [46] e.g.), where $\alpha > 0$ is a material constant, T is the absolute temperature, E_0 is an activation energy and A is a mean-collision number arising in Arrhenius law, see details in Ref. [2], e.g. f_1 is a scenario-switching factor describing the influence of relative humidity $c_w := RH$ on the reaction

$$f_1(c_w) := \begin{cases} 0, \text{ if } 0 \leq c_{w\,\min} \\ \frac{5}{2}(c_w - c_{w\,\min}), \text{ if } c_{w\,\min} < c_w \leq 0.9, \\ 1, \text{ if } 0.9 < c_w \leq 1 \end{cases}, \tag{10}$$

where $c_{w\,\min} \approx 0.5$. In the accelerated test described in Ref. [45], the relative humidity is fixed to $c_w = 0.65$. The other factors defining η_{Rv} are:
$f_2(\bar{b}) := 1 - \left(\frac{\bar{b}}{\bar{b}_{\max}}\right)^{r_1}$, $r_1 = const. > 0$. $\bar{b}_{\max}$=const.[1]> 0. Cf. Ref. [41], one usually considers $r_1 = 1$.

$f_3(\bar{c}) := \frac{\bar{c}}{\bar{c}_{\max}}$ with $c_{\max} > 0$.

$f_4(\bar{h}) := \bar{h}^{r_2}$, $r_2 \in [0, 2]$ is the newly introduced factor. We remark that if $r_2 = 0$, then (10) is the ansatz used by Wittmann et al (Ref. [21]), Saetta et al (Refs. [41, 42]) and Steffens et al (Refs. [46, 47]), e.g.

This implies the following production rate by reaction in $\Omega_1(t)$:

$$f_{\bar{b}reac1} := f_{\bar{w}reac1} := -f_{\bar{c}reac1} := f_{\bar{h}reac1} := \chi_{\Omega_1(\cdot)} \eta_{Rv} \tag{11}$$

For the reaction in the layer $\Omega_\epsilon(t)$ we propose a simplified ansatz:

$$\epsilon-\text{layer reaction rate for (1)} :=: \eta_{R\epsilon} = \kappa_{R\Gamma\epsilon} \bar{c}^p \bar{h}^q, p, q \geq 0, \quad \kappa_{R\Gamma\epsilon} := \text{ rate constant}, \tag{12}$$

where $\kappa_{R\Gamma\epsilon} = \kappa'_{R\Gamma\epsilon} A \exp(-\frac{E_0}{RT})$. The case $p = q = 1$ corresponds to the usual mass-action-law hypothesis. This implies for the production rates by reaction in $\Omega_1(t)$:

$$f_{\bar{b}reac\epsilon} := f_{\bar{w}reac\epsilon} := -f_{\bar{c}reac\varepsilon} := f_{\bar{h}reac\epsilon} := \chi_{\Omega_1(\cdot)} \eta_{R\epsilon}. \tag{13}$$

The main reason for introducing p and q is the following: In section 4 we look into the limit case $\epsilon \to 0$. The mass-action law based rate is formally derived for reactions taking place in volumes of dimensions *exceeding* the mean free path length of the particles by a factor

[1]Within this frame we consider $\bar{c}_{\max} = \lambda_{CO_2 out}$ and $\bar{b}_{\max} = 0.08324(\text{gcm}^{-3})$. $\bar{b}_{\max}$ represents the maximum amount of CO_2 which may be consumed by reaction (the degree of hydration is supposed to be about 0.8). $\bar{c}_{\max}$ is taken to be the concentration of CO_2(g) from the carbonation chamber.

essentially bigger than 1. Clearly this is not the case if ε is sufficiently small. Having no theoretical alternative, we try to adapt to the situation by allowing $p, q \neq 1$.

In order to study the influence of the reaction in $\Omega_1(t)$ vs. the one in $\Omega_\varepsilon(t)$, the total production by reaction (1) will be a weighted sum of the individual production rates:

$$f_{Ereac} := \underbrace{\delta_{1}\chi_{\Omega_1(\cdot)} f_{Ereac1}}_{\text{concentrated on } \Omega_1(t)} + \underbrace{\delta_\varepsilon \chi_{\Omega_\varepsilon(\cdot)} f_{Ereac\varepsilon}}_{\text{concentrated on } \Omega_\varepsilon(t)}, E := \overline{b}, \overline{c}, \overline{h}, \overline{w}, \delta_k \geq 0, k = 1, \epsilon, \tag{14}$$

where α and $\kappa'_{R\Gamma e}$ (cf. (11), (13)) are experimental parameters (cf. Refs. [42, 46, 29]) available only in a certain range. Varying δ_k $(k = 1, \epsilon)$ can be understood as varying $\delta_1\alpha$ and $\delta_\varepsilon\kappa'_{R\varepsilon}$, respectively. In section 5 we will study the cases $\frac{\delta_\varepsilon}{\delta_1} \ll 1$ and $\frac{\delta_\varepsilon}{\delta_1} \gg 1$.

3.2.2 Exchange between dry and wet parts of the pores

In some approaches the reaction (1) is considered as taking place at the *interface* between the water-filled parts of the pores and the dry part. Then there is no need for an extra pde for $CO_2(aq)$, since the interface approach leads at the pore level (!) to a sink term for $CO_2(g)$ which can directly be coupled with the reaction rate (cf. Refs. [35, 43]). The corresponding result is a modified production-by-reaction rate (at the macroscopic level) incorporating reaction and the idea that the reaction takes place at the interface between Ω_{pw} and Ω_{pa}. If one thinks of the reaction (1) as taking place *in* (some part of) Ω_{pw} then one has to take the exchange of $CO_2(g) \rightleftarrows CO_2(aq)$ into account. Here this will be done by Henry-law-type exchange terms:

$$f_{\overline{d}Henry} := -f_{\overline{c}Henry} = -P_H(Q_H\overline{d} - \overline{c}) \text{ on } \Omega_1(t) \cup \Omega_\varepsilon(t). \tag{15}$$

3.2.3 Dissolution and precipitation

Dissolution of $Ca(OH)_2$ takes place in all of Ω as long as there is dissolvable $Ca(OH)_2$. If at time $t = 0$ *all* dissolvable $Ca(OH)_2$ is in solution, then the corresponding dissolution source $f_{\overline{h}_k diss}, k = 1, 2$ vanishes. Otherwise, the simplest assumption is that of instantaneous (or constant) dissolution, i.e. $f_{\overline{h}_k diss} = Q_{\overline{h}_k diss} := const$. In this note we model dissolution by the deviation from equilibrium, i.e.

$$f_{\overline{h}_k diss} = P_{\overline{h}_k diss}(\overline{h}_k - \overline{h}_{eq}),\ k = 1, 2, \tag{16}$$

(cf. Ref. [28] for a thorough discussion about dissolution in concrete) as long as there is material to dissolve. In order to simplify the notations, we consider that $f_{\overline{h}_1 diss} = f_{\overline{h}_\epsilon diss}$ in $\Omega_1(t) \cup \Omega_\epsilon(t)$.

It is reported (cf., e.g., Ref. [11]) that precipitation of $CaCO_3$(aq) is very fast. We simplify this to *instantaneous*, i.e.

$$f_{\overline{b}_w preck} := -f_{\overline{b}_s preck} := -f_{\overline{h}reac} \text{ in } \Omega_k,\ k = 1, \epsilon. \tag{17}$$

Therefore, the net precipitation rate is

$$f_{\overline{b}prec} = \delta_1\chi_{\Omega_1(\cdot)} f_{\overline{h}reac1} + \delta_\epsilon\chi_{\Omega_\epsilon(\cdot)} f_{\overline{h}reac\epsilon} \text{ in } \Omega_1(t) \cup \Omega_\epsilon(t). \tag{18}$$

3.3 Transport

Transport is modeled by Fick's law, i.e. if u_E:=$[E]$, denotes the concentration of species E, then the flux of E is

$$j_E = -D_E \nabla u_E, \tag{19}$$

where D_E is the effective diffusion coefficient of species E in concrete. See, e.g., Refs. [35, 36, 37]. We note that the effective diffusion coefficient D_{CO_2} might be expressed as $D_{CO_2} = D_{O_2} f_{diff}$, where D_{O_2} is the effective diffusion coefficient of O_2 in concrete and f_{diff} is a correction factor taking the influence of porosity, temperature and carbonation degree into account (cf. Refs. [3, 46] or Ref. [42] for a simpler setting).

3.4 Two inner-interface conditions at $\Gamma_r(t)$

The uncarbonated area is separated from the rest of Ω by $\Gamma_r(t)$. This is the place where CO_2 might suffer a drop. Furthermore, we assume no CO_2-influx into $\Omega_2(t)$ - since otherwise there could be carbonation going on in $\Omega_2(t)$. This yields the following Rankine-Hugoniot type boundary condition at $x + \frac{\epsilon}{2} n(x) \in \Gamma_r(t)$ (cf. Ref. [9]):

$$j_E(x + \frac{\epsilon}{2} n(x), t) \cdot n(x) = E(x + \frac{\epsilon}{2} n(x), t) \dot{s}(x, t) \text{ for all } x \in \Gamma(t), t > 0, E = \overline{c}, \overline{d} \tag{20}$$

The time derivative $\dot{s}(x,t)$ denotes the speed of progression of the carbonation-reaction layer $\Omega_\epsilon(t)$ in the direction of the normal $n(x)$ at $x \in \Gamma(t)$, measured at the middle line (or surface) $\Gamma(t)$.

We note that, depending on one's definition of the reaction zone Ω_ϵ, the choice

$$E(x + \frac{\epsilon}{2} n(x), t) = 0, \overline{c}, \overline{d} \tag{21}$$

might be reasonable, as opposed to $\overline{c}(x,t) = 0$ for $x \in \Gamma(t)$ in the limit model ($\epsilon = 0$), where the boundary condition (21) is not reasonable, since it implies that there is no reactant available for carbonation at $\Gamma(t) = \Omega_{\epsilon=0}(t)$. Relation (21) simplifies the flux condition to

$$j_E(x + \frac{\epsilon}{2} n(x), t) \cdot n(x) = 0 \text{ for all } x \in \Gamma(t), t > 0, E = \overline{c}, \overline{d} \tag{22}$$

A further condition will be needed to complete the model, since the position of $\Gamma(t)$ is simultaneously to be determined. Balancing the amount produced by carbonation and the amount used for carbonation one obtains (cf. Ref. [9]):

$$\dot{s}(t) = \frac{1}{\int_{\Omega_\epsilon(t)} \overline{h}(x + \frac{\epsilon}{2} n(x), t) dx} \epsilon \int_{\Omega_\epsilon(t)} \eta_{R\Gamma\epsilon}(x + \frac{\epsilon}{2} n(x), t) dx \text{ for all } x \in \Gamma(t), t > 0. \tag{23}$$

3.5 Boundary conditions at the exterior boundary, Γ_{ext}, and at $x = L$

Boundary conditions on Γ_{ext} are needed for all species governed by a pde involving second space derivatives, i.e. for $\overline{c}, \overline{d}, \overline{h}$ and $\overline{w}$, respectively. If there is an oversupply of substance (like for $CO_2(g)$ in accelerated carbonation experiments or for H_2O under heavy rain), or more generally, if one can assume that at a tiny (inner) surface part of the sample the concentrations (or pressures, where applicable) are the same as outside, then one chooses Dirichlet boundary conditions, otherwise Neumann-Robin conditions are the right choice. If $D > 1$, the following setting covers both situations: We divide the boundary Γ_{ext} (cf. Fig. 3) in two disjoint parts $\Gamma_{ext}^{(N)}$ and $\Gamma_{ext}^{(D)}$ such that for $E = \overline{c}, \overline{d}, \overline{h}, \overline{w}$:

$$E(x,t) = \lambda_{Eout}(x,t) \text{ for } x \in \Gamma_{ext}^{(D)}, t > 0, \tag{24}$$

$$j_E(x,t) \cdot n(x) = p_E(E(x,t) - \lambda_{Eout}(x,t)) \text{ for } x \in \Gamma_{ext}^{(N)}, t > 0, \tag{25}$$

where p_E denotes a mass-transfer coefficient depending on species E and surface $\Gamma_{ext}^{(N)}$.

In the sequel we restrict ourselves to Dirichlet-boundary conditions at Γ_{ext}. By symmetry one has to require

$$j_E(x,t) \cdot n(x) = 0, \text{ at } x = L. \tag{26}$$

3.6 Initial conditions

The initial position of $\Gamma(t)$, denoted by $\Gamma(0)$, and the initial concentrations

$$E(x,0) = E_0(x), x \in \Omega, \ E = \overline{c}, \overline{d}, \overline{h}, \overline{w}, \tag{27}$$

as well as the initial amount of carbonatable $Ca(OH)_2(s)$ (before dissolution starts!), $m^*_{Ca(OH)_2(s)}$, are supposed to be known (cf. appendix).

3.7 The model $(P_{2\epsilon})$

Let $\epsilon > 0$. The balance equations in section 3.1, the production terms in 3.2, the interface, boundary and initial conditions in 3.4 - 3.6 and the flux law in 3.3 will be summarized as model $(P_{2\epsilon})$. The solution vector $\overline{X} := (\overline{b}, \overline{c}, \overline{d}, \overline{h}, \overline{w}, \Gamma)$ will be called the model *output*. If the setting is $1D$, then $\Gamma(t)$ can be identified by its position $s(t)$. In this case $\overline{X} := (\overline{b}, \overline{c}, \overline{d}, \overline{h}, \overline{w}, s)$ will be called the model output.

4 The limit case $\epsilon \to 0$ (surface-concentrated reaction + volume reaction)

This short section is a purely academic digression. In Ref. [9] we discussed the case $\epsilon \to 0$, for the following setting (a)-(c):

(a) There is no $Ca(OH)_2$ in $\Omega_1(t)$ and no CO_2 in $\Omega_2(t)$,
(b) The carbonation reaction (1) takes place only in $\Omega_\varepsilon(t)$ (as a volume reaction) or
(c) Reaction (1) takes place only on $\Gamma(t)$ (as a surface reaction).

Loosely speaking it turns out that (numerically as well as theoretically) (a) + (c) provides the limit case of (a) + (b) as $\epsilon \to 0$.

In some way there are two limit cases for $\epsilon \to 0$. One models the carbonation reaction as a process taking place solely in the interior of $\Omega_1(t)$, the other one considers (1) as a reaction in $\Omega_1(t)$ plus a reaction concentrated on $\Gamma(t)$.

In order to make this more precise, let $\overline{X}_\varepsilon := (\overline{b_\varepsilon}, \overline{c_\varepsilon}, \overline{d_\varepsilon}, \overline{h_\varepsilon}, \overline{w_\varepsilon}, s_\varepsilon)$ denote the solution of model $(P_{2\epsilon})$ and assume for simplicity $f_{ERv} := 0$, keep the *structure* and constants (with the exception of ϵ) of all material and process functions (porosities, diffusion coefficients, the initial concentrations, the initial position of $\Gamma, \Gamma(0)$, and the boundary setting at Γ_{ext} as well as the the source and sink terms f_E, with the exception of the reaction terms for Ω_ϵ, $f_{Ereac\varepsilon}$, fixed.
Let ΔV be a control volume, $S' := (t, t + \Delta t]$ a time interval. $\int_{S'} \int_{\Delta V \cap \Omega_\varepsilon(\tau)} f_{Ereac\varepsilon} dx d\tau$ represents the amount of substance associated with the concentration E which is produced by carbonation during S' in ΔV. Under reasonable mathematical assumptions such as uniform boundedness of the concentrations entering $f_{Ereac\varepsilon}$, it can be shown that there is a limit function $f_{Ereac\Gamma}$ verifying

$$\int_{S'} \int_{\Delta V \cap \Omega_\varepsilon(\tau)} f_{Ereac\varepsilon} dx d\tau \overset{\varepsilon \to 0}{\to} \int_{S'} \int_{\Delta V \cap \Gamma(\tau)} f_{Ereac\Gamma} dx d\tau \quad \text{for all control volumes } \Delta V.$$

Interpreting $f_{Ereac\Gamma}$ as a surface production density, it means that for small ε the production on Ω_ε (here: reaction (1)) can be approximated by a reaction on Γ. Note that, under mild *mathematical* assumptions, this implies $\varepsilon f_{Ereac\varepsilon} \overset{\varepsilon \to 0}{\to} f_{Ereac\Gamma}$. This fact yields information on the behaviour of the concentrations near Γ of the species entering $f_{Ereac\varepsilon}$, if one *wants* to approximate model $(P_{2\epsilon})$ by a model with $\Gamma(t)$-concentrated reactions. Such an attempt could be motivated by numerical advantages or others. The two cases mentioned above are $f_{Ereac\Gamma} = 0$ (no production on Γ) and $f_{Ereac\Gamma} \neq 0$.
Note that the solution output $\overline{X}_\varepsilon := (\overline{b_\varepsilon}, \overline{c_\varepsilon}, \overline{d_\varepsilon}, \overline{h_\varepsilon}, \overline{w_\varepsilon}, s_\varepsilon)$ also converges to a solution $\overline{X} := (\overline{b}, \overline{c}, \overline{d}, \overline{h}, \overline{w}, s)$ of the corresponding problem $(P_{2\epsilon=0})$ (with the volume rate $f_{Ereac\varepsilon}$ replaced by the surface reaction rate $f_{Ereac\Gamma}$ (cf. Ref. [9]).

5 Simulation results for model $(P_{2\epsilon})$

5.1 Simulation strategy

In our simulations we will address the following questions:

1. How does a change of the *structure* of the reaction rate (exemplified by p, q, r_1, r_2 (cf. (13)) affects the output?

2. How does a change of the width ϵ of the main carbonation zone Ω_ϵ affects the output?

3. How does a change of the weight of the reactions in Ω_1 and Ω_ϵ, respectively, affects the output? Recall: A way of weighing is given by the weights δ_1 and δ_ϵ in (15). We will discuss several cases of $\delta = \frac{\delta_\epsilon}{\delta_1} \gg 1$ and $\delta \ll 1$.

4. Does the model reproduce some of the characteristics which are standard expectations for carbonation such as the $\sqrt{t}$-law for the penetration depth (for large t) or others?

5. Is the two-reaction-zones model $(P_{2\epsilon})$ capable of reproducing experimental results? More precisely: Let $r_1 = 0$ in (13), fix all data except p and q in (13) and α in (9). Are there reasonable p, q, α such that the simulation-output of model $(P_{2\epsilon})$ comes close to measurement data?

5.2 Outline of the simulation of model $(P_{2\epsilon})$

Applying a fixing boundary technique [Landau (1950)] we transform the moving boundary problem $(P_{2\epsilon})$ into a problem with fixed boundaries. The price of this transformation is paid by obtaining space- and time- dependent coefficients in the transformed equations. By means of the weak formulation of the transformed problem together with a (piecewise linear) spline-based Galerkin ansatz, we obtain a system of $5n+1$ ode's which we solve. Section 5.4 contains several numerical tests and their evaluation with respect to the chemical-physical mechanisms that usually appear in the carbonation of concrete-based materials.

5.3 Simulation procedure for $(P_{2\epsilon})$

We make use of the change of variable

$$y = \begin{cases} \frac{x}{s(t)+\frac{\epsilon}{2}}, & \text{if } x \in [0, s(t)+\frac{\epsilon}{2}] \\ \\ \frac{L-x}{L-s(t)-\frac{\epsilon}{2}}, & \text{if } x \in [s(t)-\frac{\epsilon}{2}, L] \end{cases} \tag{28}$$

to transform the domains $\Omega_1(t) \cup \Omega_\epsilon(t)$ and $\Omega_2(t)$ into the intervals $[l_{1\epsilon}, 1]$ and $[0, 1]$, respectively, where $l_{1\epsilon} = 1 - \frac{\epsilon}{s(t)+\frac{\epsilon}{2}}$ represents the image of the point $x = s(t) - \frac{\epsilon}{2}$ through the transformation (28).

After setting $c(y,t) = \bar{c}(x,t) - \lambda_{\bar{c}}$, $d(y,t) = \bar{d}(x,t) - \lambda_{\bar{d}}$, $h_1(y,t) = \bar{h}_1(x,t) - \lambda_{\bar{h}_1}$, $h_2(y,t) = \bar{h}_2(x,t) - \lambda_{\bar{h}_2}$ and $b(y,t) = \bar{b}(x,t) - \lambda_{\bar{b}}$, we homogenize the Dirichlet boundary conditions (24) prescribed in section 3.5. Using transformation (28), we obtain a system of equations on the fixed domain $0 < y < 1$. Therefore, the model $(P_{2\epsilon})$ (summarized in section 3.7) can be rewritten as:

$$c_{,t} = \frac{D_{c_2}}{\left(s(t)+\frac{\epsilon}{2}\right)^2} c_{,yy} + \frac{\dot{s}(t)}{s(t)+\frac{\epsilon}{2}} y c_{,y} + f_{\bar{c}Henry} + \delta_1 \chi_{[0,l_{1\epsilon})} f_{\bar{c}reac1} + \delta_\epsilon \chi_{[l_{1\epsilon},1]} f_{\bar{c}reac\epsilon}, t > 0, \tag{29}$$

$$d_{,t} = \frac{D_{d_1}}{\left(s(t)+\frac{\epsilon}{2}\right)^2} d_{,yy} + \frac{\dot{s}(t)}{s(t)+\frac{\epsilon}{2}} y d_{,y} + f_{\bar{d}Henry}, t > 0, \tag{30}$$

$$h_{1,t} = \frac{D_{h_1}}{\left(s(t)+\frac{\epsilon}{2}\right)^2} h_{1,yy} + \frac{\dot{s}(t)}{s(t)+\frac{\epsilon}{2}} y h_{1,y} + f_{\bar{h}_1 diss} + \delta_1 \chi_{[0,l_{1\epsilon})} f_{\bar{h}_1 reac1} + \delta_\epsilon \chi_{[l_{1\epsilon},1]} f_{\bar{h}_1 reac\epsilon}, t > 0, \tag{31}$$

$$h_{2,t} = \frac{D_{h_2}}{\left(s(t)+\frac{\epsilon}{2}-L\right)^2} h_{2,yy} + \frac{\dot{s}(t)}{s(t)+\frac{\epsilon}{2}-L} y h_{2,y} + f_{\bar{h}_2 diss}, t > 0, \tag{32}$$

$$b_{,t} = \frac{\dot{s}(t)}{s(t)+\frac{\epsilon}{2}} y b_{,y} + \delta_1 \chi_{[0,l_{1\epsilon})} f_{\bar{b}reac1} + \delta_\epsilon \chi_{[l_{1\epsilon},1]} f_{\bar{b}reac\epsilon}, t > 0. \tag{33}$$

Letting $\bar{c}(y,0) = \lambda_{\bar{c}}, \bar{d}(y,0) = \lambda_{\bar{d}}, \bar{h}_1(y,0) = \lambda_{\bar{h}_1}, \bar{h}_2(y,0) = \lambda_{\bar{h}_2}$ and $\bar{b}(y,0) = \lambda_{\bar{b}}$, the initial conditions in 3.6 transform into:

$$c(y,0) = 0,\ d(y,0) = 0,\ h_1(y,0) = 0,\ h_2(y,0) = 0 \text{ and } b(y,0) = 0. \tag{34}$$

The boundary conditions associated to the model $(P_{2\epsilon})$ (cf. sections 3.4, 3.5 and 3.6) become

$$c(0,t) = 0, \quad -\frac{D_{c_1}}{s(t)+\frac{\epsilon}{2}} c_{,y}(1,t) = \dot{s}(t)\left(c(1,t) + \lambda_{\bar{c}}\right), t > 0, \tag{35}$$

$$d(0,t) = 0, \quad -\frac{D_{d_1}}{s(t)+\frac{\epsilon}{2}} d_{,y}(1,t) = \dot{s}(t)\left(d(1,t) + \lambda_{\bar{d}}\right), t > 0, \tag{36}$$

$$h_1(0,t) = 0, \quad \frac{D_{h_1}}{s(t)+\frac{\epsilon}{2}} h_{1,y}(1,t) = \frac{D_{h_2}}{s(t)+\frac{\epsilon}{2}-L} h_{2,y}(1,t) \text{ and } h_2(0,t) = 0, t > 0. \tag{37}$$

Interface condition (24) turns into

$$\dot{s}(t) = \frac{\int_{\Omega_\epsilon(t)} \bar{\eta}_{\Gamma\epsilon}(x,t) dx}{\frac{1}{\epsilon}\int_{\Omega_\epsilon(t)} \left(h_1(x,t) + \lambda_{\bar{h}_1}\right) dx}, \tag{38}$$

where $t > 0$, $0 < y < 1$ and

$$s(0) = s_0. \tag{39}$$

To solve the system (29)-(39) numerically, we use its weak formulation and a (piecewise) linear-based Galerkin scheme. Let $\{\psi_j^n\}_{j=0}^n$ denote the standard piecewise linear splines on the interval $[0,1]$ defined with respect to the uniform mesh $[0, \frac{1}{n}, \frac{2}{n}, \ldots, 1]$. That is, for a fixed $n \in \mathbb{N} - \{0\}$ and $j = 0, 1, 2, \ldots, n$, we introduce

$$\psi_j^n(y) = \begin{cases} 1 - |ny - j|, & \text{if } y \in \left[\frac{j-1}{n}, \frac{j+1}{n}\right] \cap [0,1] \\ 0, & \text{elsewhere on } [0,1]. \end{cases}$$

To obtain the Galerkin system, we set

$$\begin{aligned} c^n(y,t) &= \textstyle\sum_{j=1}^n C_j^n(t)\psi_j^n(y), \quad d^n(y,t) = \sum_{j=1}^n D_j^n(t)\psi_j^n(y), \\ h_k^n(y,t) &= \textstyle\sum_{j=1}^n H_{kj}^n(t)\psi_j^n(y), \quad b^n(y,t) = \sum_{j=1}^n B_j^n(t)\psi_j^n(y) \end{aligned} \tag{40}$$

with $k = 1, 2$, $t \geq 0, 0 \leq y \leq 1$ where

$$C^n(t) = [C_1^n(t), C_2^n(t), \ldots, C_n^n(t)]^T \in \mathbb{R}^n, \qquad D^n(t) = [D_1^n(t), D_2^n(t), \ldots, D_n^n(t)]^T \in \mathbb{R}^n,$$

$$H_k^n(t) = [H_{k1}^n(t), H_{k2}^n(t), \ldots, H_{kn}^n(t)]^T \in \mathbb{R}^n, \quad B^n(t) = [B_1^n(t), B_2^n(t), \ldots, B_n^n(t)]^T \in \mathbb{R}^n.$$

The superscript T stands for transposition.

The Galerkin equations are given by

$$\begin{aligned}
M^n\dot{C}^n(t) = \; & -\tfrac{D_{c_1}}{\left(s^n(t)+\frac{\epsilon}{2}\right)^2}K^nC^n(t) + \tfrac{\dot{s}^n(t)}{s^n(t)+\frac{\epsilon}{2}}L_l^nC^n(t) - \tfrac{\dot{s}^n(t)}{s^n(t)+\frac{\epsilon}{2}}\left(C_n^n(t)+\lambda_{\bar{c}}\right)e^n + \\
& + P_H\left(Q_HM^nD^n(t) - M^nC^n(t)\right) + P_H\left(Q_H\lambda_{\bar{d}}^n - \lambda_{\bar{c}}^n\right) + \\
& + \delta_1 f_{\bar{c}reac1}^n(t) + \delta_\epsilon f_{\bar{c}reac\epsilon}^n(t), \; t > 0, \\
M^n\dot{D}^n(t) = \; & -\tfrac{D_{d_1}}{\left(s^n(t)+\frac{\epsilon}{2}\right)^2}K^nD^n(t) + \tfrac{\dot{s}^n(t)}{s^n(t)+\frac{\epsilon}{2}}L_l^nD^n(t) - \tfrac{\dot{s}^n(t)}{s(t)+\frac{\epsilon}{2}}\left(D_n^n(t)+\lambda_{\bar{d}}\right)e^n - \\
& - P_H\left(Q_HM^nD^n(t) - M^nC^n(t)\right) - P_H\left(Q_H\lambda_{\bar{d}}^n - \lambda_{\bar{c}}^n\right), \; t > 0, \\
M^n\dot{H}_1^n(t) = \; & -\tfrac{D_{h_1}}{\left(s^n(t)+\frac{\epsilon}{2}\right)^2}K^nH_1^n(t) + \tfrac{\dot{s}^n(t)}{s^n(t)+\frac{\epsilon}{2}}L_l^nH_1^n(t) - \tfrac{D_{h_1}}{\left(s^n(t)+\frac{\epsilon}{2}\right)^2}\left(H_{1n}^n(t)+\lambda_{\bar{h}_1}\right)e^n + \\
& + \delta_1 f_{\bar{h}_1reac1}^n(t) + \delta_\epsilon f_{\bar{h}_1reac\epsilon}^n(t), \; t > 0, \\
M^n\dot{H}_2^n(t) = \; & -\tfrac{D_{h_2}}{(s^n(t)+\frac{\epsilon}{2}-L)^2}K^nH_2^n(t) + \tfrac{\dot{s}^n(t)}{s^n(t)+\frac{\epsilon}{2}-L}L_l^nH_2^n(t) - \tfrac{D_{h_2}}{\left(s^n(t)+\frac{\epsilon}{2}-L\right)^2}\left(H_{2n}^n(t)+\lambda_{\bar{h}_2}\right)e^n - \\
& + S_{h2diss}P_{h2diss}M^nH^n(t), \; t > 0, \\
M^n\dot{B}^n(t) = \; & \tfrac{\dot{s}^n(t)}{s^n(t)+\frac{\epsilon}{2}}L_l^nB^n(t) + +\delta_1 f_{\bar{b}reac1}^n(t) + \delta_\epsilon f_{\bar{b}reac\epsilon}^n(t), t > 0,
\end{aligned} \tag{41}$$

where $f_{\bar{c}reac1}^n(t) = f_{\bar{h}_1reac1}^n(t) = -f_{\bar{b}reac1}^n(t)$ and

$$f_{\bar{b}reac1}^n(t) = \frac{\bar{\alpha}}{\bar{b}_{max}^{r_1}\bar{c}_{max}}\int_0^1 \left(\bar{b}_{max}^{r_1} - (b^n(y,t)+\lambda_{\bar{b}})^{r_1}\right)(c^n(y,t)+\lambda_{\bar{c}})\left(h_1^n(y,t)+\lambda_{\bar{h}_1}\right)^{r_2}\psi^n(y)dy,$$

with $r_1 > 0$, $r_2 \in [0, 2]$ and

$$\bar{\alpha} := \alpha A e^{-\frac{E_Q}{RT}} f_1(RH) \tag{42}$$

is a material parameter (cf. section 3.2.1).
Also, we set $f_{\bar{c}reac\epsilon}^n(t) = f_{\bar{h}_1reac\epsilon}^n(t) = -f_{\bar{b}reac\epsilon}^n(t)$, where

$$f_{\bar{b}reac\epsilon}^n(t) = k\int_0^1 (c^n(y,t)+\lambda_{\bar{c}})^p\left(h_1^n(y,t)+\lambda_{\bar{h}_1}\right)^q\psi^n(y)dy, t > 0.$$

The interface relation (38) becomes[2]:

$$\dot{s}^n(t) = \bar{k}\epsilon \frac{\int_{l_{1\epsilon}}^1 \left(c^n(y,t) + \lambda_{\bar{c}}\right)^p \left(h_1^n(y,t) + \lambda_{\bar{h}_1}\right)^q dy}{\int_{l_{1\epsilon}}^1 \left(h_1^n(y,t) + \lambda_{\bar{h}_1}\right) dy}, \tag{43}$$

where $t > 0, p, q \in [0,2]$, and

$$s^n(0) = s_0 \geq d_{10} + \frac{\epsilon}{2} > 0. \tag{44}$$

d_{10} denotes the width[3] of the initial layer Ω_{10}. See the reference picture Fig. 6.

The initial conditions are

$$C^n(0) = 0, D^n(0) = 0, H_1^n(0) = 0, H_2^n(0) = 0 \text{ and } B^n(0) = 0. \tag{45}$$

Remark 1 The matrices $M^n,\ K^n \in \mathbb{R}^{(n+1)\times(n+1)},\ L_l^n \in \mathbb{R}^{n\times n}$ and $e^1, e^n, \lambda_{\bar{c}}^n, \lambda_{\bar{d}}^n \in \mathbb{R}^n$, $n \in \mathbb{N}, n > 1$ are given by

$$[M^n]_{ij} = \int_0^1 \psi_i^n(y)\psi_j^n(y)dy,\ [K^n]_{ij} = \int_0^1 \psi_i^{n\prime}(y)\psi_j^{n\prime}(y)dy,\ i,j = 1,2,\ldots,n+1,$$

$$[L_l^n]_{ij} = \int_0^1 y\psi_i^n(y)\psi_j^{n\prime}(y)dy,\ i,j = 1,2,\ldots,n$$

and

$$e^1 = [1,\ 0,\ \ldots\ ,0,\ 0]^T, \quad e^n = [0,\ 0,\ \ldots\ ,0,\ 1]^T,$$

$$\lambda_{\bar{c}}^n = \lambda_{\bar{c}}\left[\frac{1}{n}, \frac{1}{n}, \ldots, \frac{1}{n}, \frac{1}{2n}\right]^T, \quad \lambda_{\bar{d}}^n = \lambda_{\bar{d}}\left[\frac{1}{n}, \frac{1}{n}, \ldots, \frac{1}{n}, \frac{1}{2n}\right]^T.$$

The stiffness matrix M^n is sparse, symmetric, positive definite and diagonally dominant. We note that $cond(M^n) \approx 3.9938$ for $n = 32$ and $cond(M^n) \approx 3.9993$ for $n = 100$. We used MATLAB routine `ode15s` to integrate the system of ode's (41), (43) with the initial values (44), (45).

[2]The factor $\bar{k} = \frac{k}{\alpha_1}$ (k is given in Ref. [29]) accounts for the effect of the variation of exponents p, q on the carbonation rate constant k. Since we are not aware of experimental data for such effect, a (possible) threshold value for this parameter is found numerically by variation of the value of an auxiliary parameter $\alpha_1 > 0$. Once better measurements of carbonation rate constant are available, the parameter α_1 can be identified.

[3]In the simulations we chose $s_0 = d_{10} + \frac{\epsilon}{2}$ with $d_{10} = 10^{-1}$.

5.4 Simulation curves

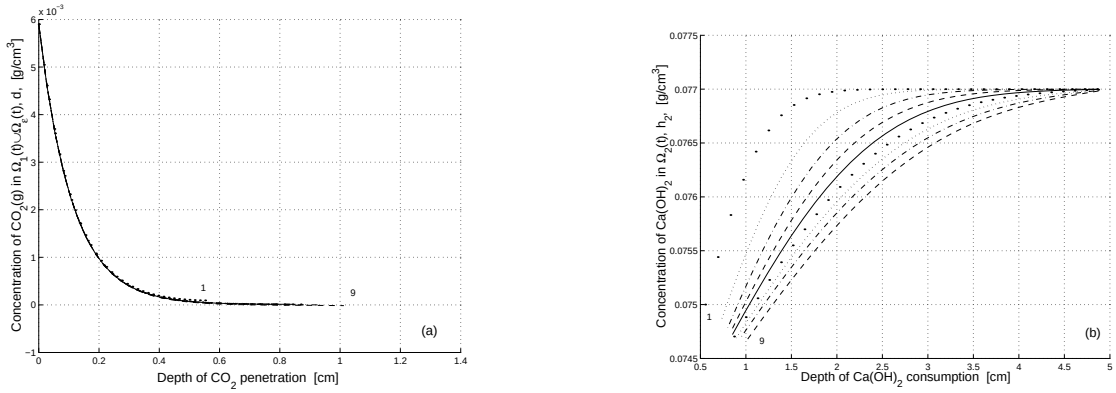

Figure 7: (a) Profiles of CO_2(g) in $\Omega_1(t) \cup \Omega_\epsilon(t)$. One observes that the exposure concentration of CO_2(g) was split via Henry's law in the initial layer. CO_2 is strongly consumed in $\Omega_\epsilon(t)$. (b) Profiles of $CaOH_2$ in $\Omega_2(t)$. $(D_{d_1}, k, \alpha_1, p, q, r_1, r_2, \epsilon) = (3.5, 5 \times 10^3, 10^2, 2, 0.5, 1, 1, \frac{1}{10})$ and $\frac{\delta_\epsilon}{\delta_1} \ll 1$.

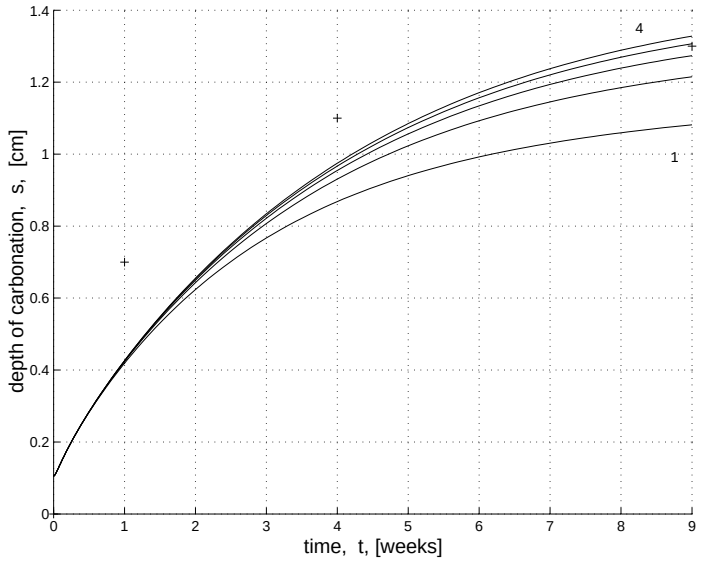

Figure 8: Carbonation penetration (in cm) after 9 weeks of accelerated testing. The graphs were obtained varying $\delta_1 = \frac{\delta_0}{2}, \frac{\delta_0}{4}, \frac{\delta_0}{6}, \frac{\delta_0}{8}, \frac{\delta_0}{10}$, where $\delta_0 = 10^{-5}\delta_\epsilon$. $(k, D_{d_1}, p, q, \alpha_1, r_1, r_2, \epsilon) = (5 \times 10^3, 3.5, 2, 0.5, 10^2, 1, 1, \frac{1}{100})$ in the case $\frac{\delta_\epsilon}{\delta_1} \gg 1$.

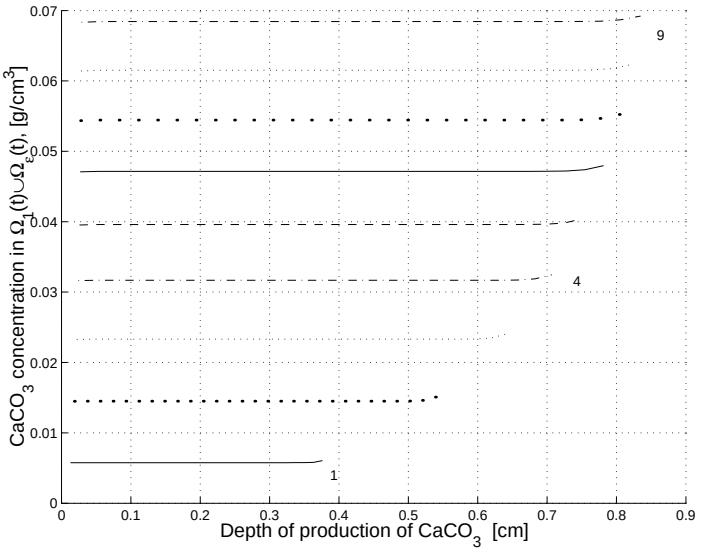

Figure 9: $CaCO_3$ concentration in $\Omega_1(t) \cup \Omega_\epsilon(t)$ after 9 weeks of accelerated testing. One observes that after each time interval (7 days) some calcium carbonate is produced. This production stops when all available $Ca(OH)_2$ in $\Omega_1(t) \cup \Omega_\epsilon(t)$ is consumed. Here $(k, D_{d_1}, p, q, \alpha_1, r_1, r_2, \epsilon) = (5 \times 10^3, 3.5, 2, 0.5, 10^2, 1, 1, \frac{1}{100})$ and $\frac{\delta_\epsilon}{\delta_1} \gg 1$.

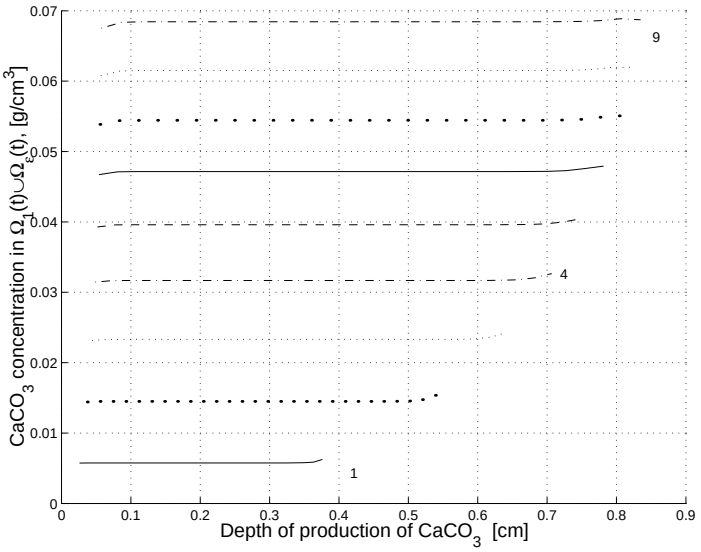

Figure 10: $CaCO_3$ concentration in $\Omega_1(t) \cup \Omega_\epsilon(t)$ after 9 weeks of accelerated testing. Here $(k, D_{d_1}, p, q, \alpha_1, r_1, r_2, \epsilon) = (5 \times 10^3, 3.5, 2, 0.9, 10^2, 1, 1, \frac{1}{100})$ in the case $\frac{\delta_\epsilon}{\delta_1} \gg 1$. One can remark smoothing effects produced on the concentration profiles by the introduction of an artificial diffusive flux of $CaCO_3$(aq) with $D_{b_1} = 10^{-4}$.

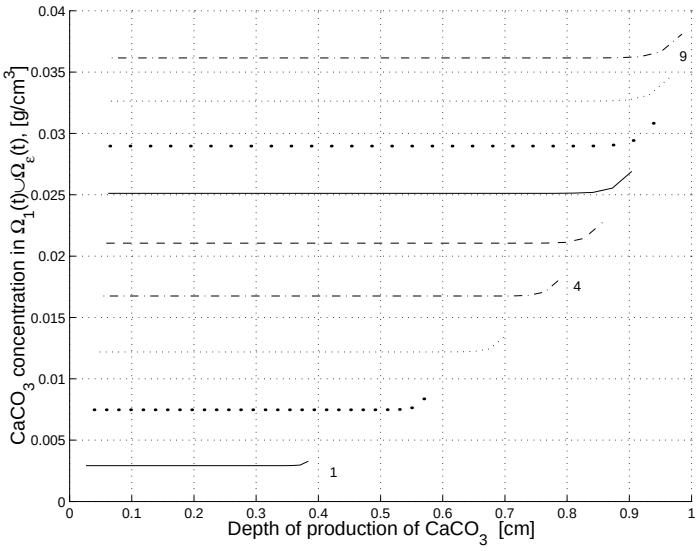

Figure 11: $CaCO_3$ concentration in $\Omega_1(t) \cup \Omega_\epsilon(t)$ after 9 weeks of accelerated testing. Here we used the same parameters as in Fig 9: $(k, D_{d_1}, p, q, \alpha_1, r_1, r_2, \epsilon) = (5 \times 10^3, 3.5, 2, 0.5, 10^2, 1, 1, \frac{1}{100})$ but with a bigger ratio $\frac{\delta_\epsilon}{\delta_1} \gg 1$ (more precisely, with a smaller δ_1).

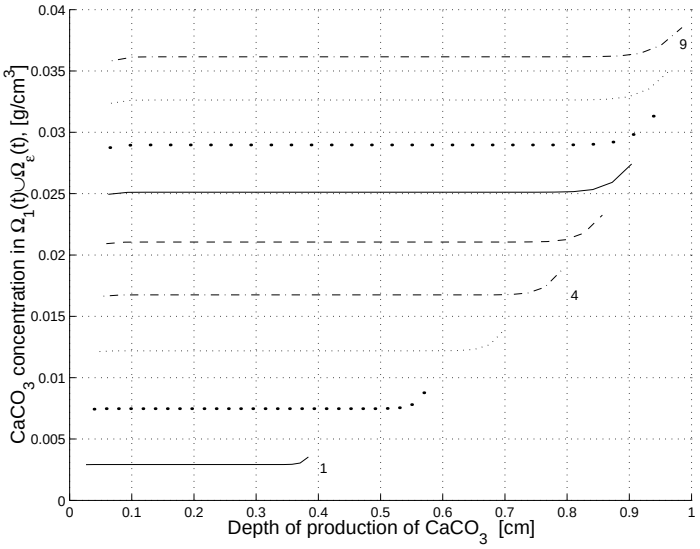

Figure 12: $CaCO_3$ concentration in $\Omega_1(t) \cup \Omega_\epsilon(t)$ after 9 weeks of accelerated testing. Here $(k, D_{d_1}, p, q, \alpha_1, r_1, r_2, \epsilon, d_{10}) = (5 \times 10^3, 3.5, 2, 0.9, 10^2, 1, 1, \frac{1}{100}, 0.1)$ in the case $\frac{\delta_\epsilon}{\delta_1} \gg 1$. One can remark smoothing effects produced on the concentration profiles by the introduction of an artificial diffusive flux of $CaCO_3$(aq) with $D_{b_1} = 10^{-4}$.

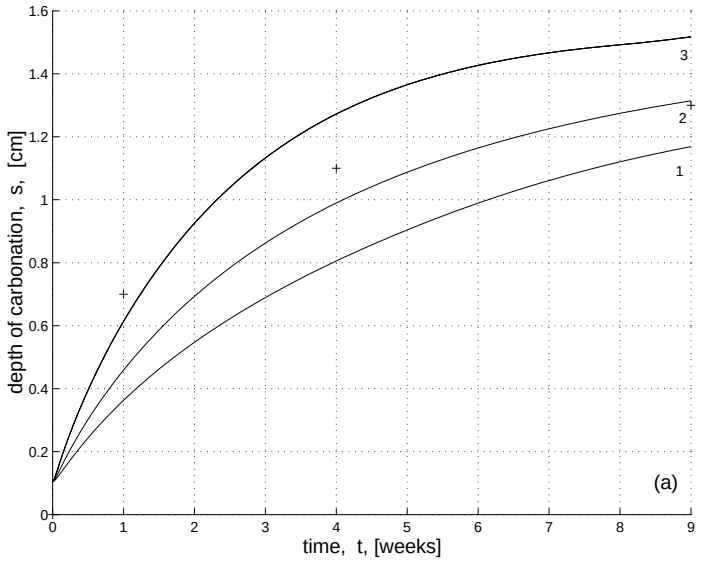

Figure 13: Carbonation penetration (in cm) after 9 weeks of accelerated testing. The graphs were obtained varying the exponents $(p, q) = (2, 0.5), (2, 0.7), (2, 0.9)$. Here $(k, D_{d_1}, \alpha_1, r_1, r_2, \epsilon) = (5 \times 10^3, 3.5, 10^2, 1, 1, \frac{1}{100})$ and $\frac{\delta_\epsilon}{\delta_1} \gg 1$.

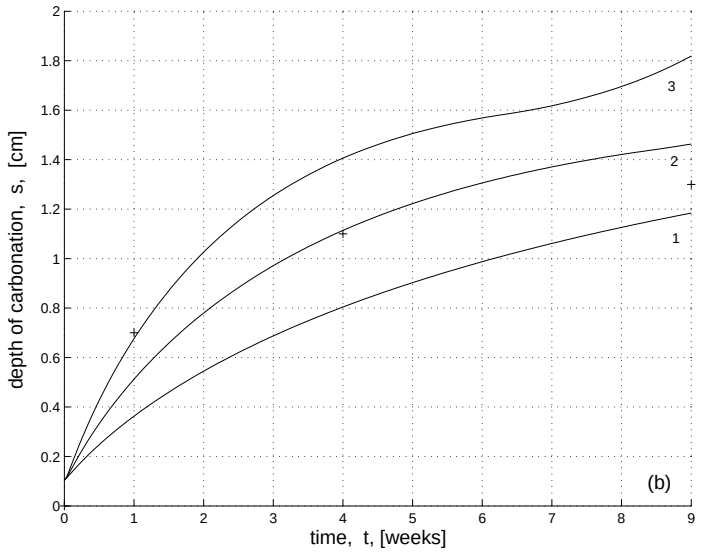

Figure 14: Carbonation penetration (in cm) after 9 weeks of accelerated testing. The graphs were obtained varying the diffusivity $D_{d_1} = \frac{14}{8}, \frac{21}{8}, \frac{28}{8}$. Here $(k, p, q, \alpha_1, r_1, r_2, \epsilon) = (5 \times 10^3, 1.8, 0.8, 10^2, 1, 1, \frac{1}{100})$ and $\frac{\delta_\epsilon}{\delta_1} \gg 1$.

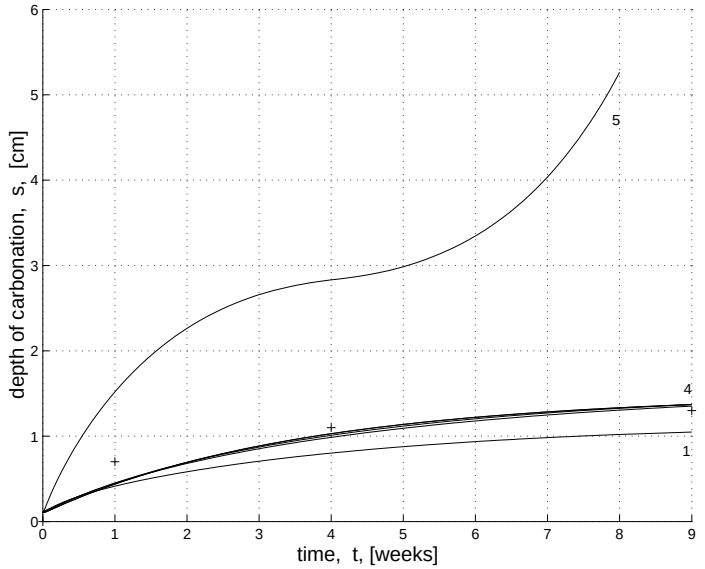

Figure 15: Carbonation penetration (in cm) after 9 weeks of accelerated testing. The graphs were obtained varying $\epsilon = \frac{1}{25}, \frac{1}{50}, \frac{1}{100}, \frac{1}{150}, \frac{1}{300}$. Here $(k, D_{d_1}, p, q, \alpha_1, r_1, r_2) = (5 \times 10^3, 3.5, 2, 0.8, 10^2, 1, 1)$ and $\frac{\delta_\epsilon}{\delta_1} \gg 1$. One observes that the bigger the ϵ is, the faster the speed becomes. $\epsilon = \frac{1}{300}$ leads to numerical instability.

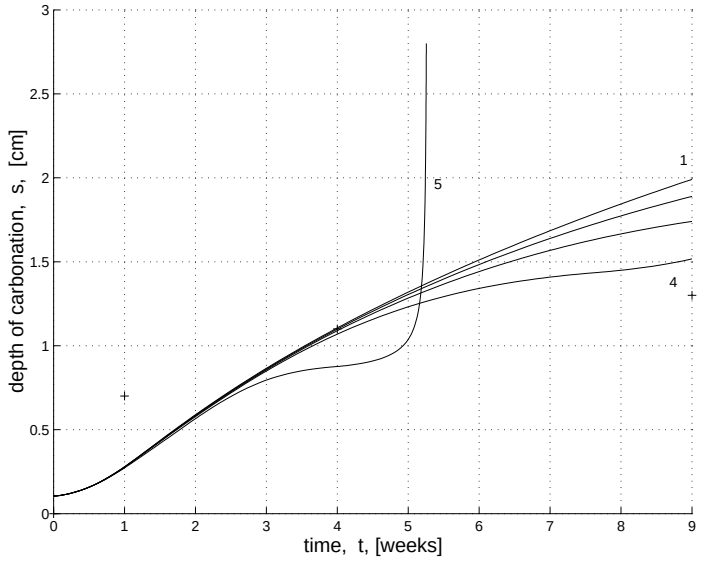

Figure 16: Carbonation penetration (in cm) after 9 weeks of accelerated testing. The graphs were obtained varying $r_2 = 0, 0.5, 0.75, 1, 1.5$. The blow up appears when $r_2 = 1.5$. $(k, D_{d_1}, p, q, \alpha_1, r_1, \epsilon) = (5 \times 10^3, 3.5, 1.8, 1.5, 10^2, 1, \frac{1}{100})$ and $\frac{\delta_\epsilon}{\delta_1} \gg 1$.

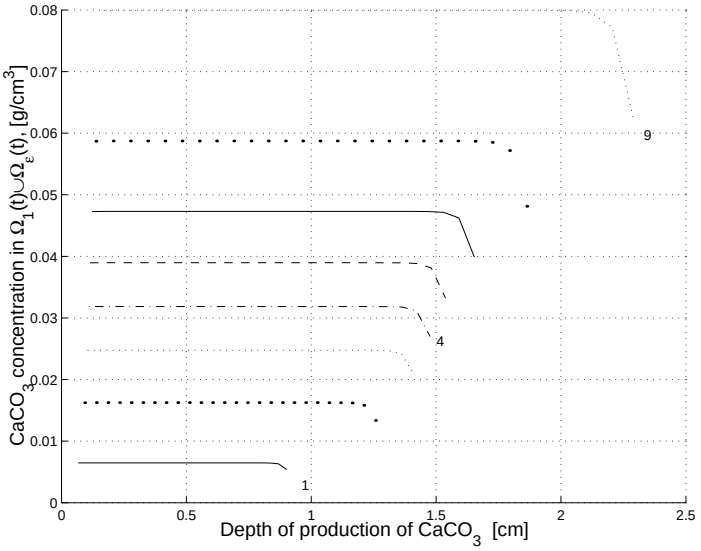

Figure 17: $CaCO_3$ concentration in $\Omega_1(t) \cup \Omega_\epsilon(t)$ after 9 weeks of accelerated testing. Here $(k, D_{d_1}, p, q, \alpha_1, r_1, r_2, \epsilon) = (5 \times 10^3, 3.5, 2, 0, 10^2, 1, 1, \frac{1}{8})$ and $\frac{\delta_\epsilon}{\delta_1} \ll 1$. Here $CaCO_3$(aq) is allowed to diffusive very slowly ($D_{b_1} = 10^{-4}$).

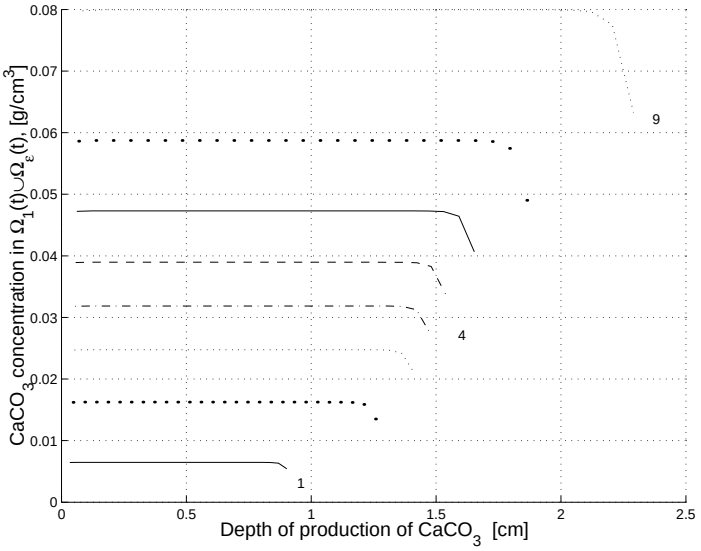

Figure 18: $CaCO_3$ concentration in $\Omega_1(t) \cup \Omega_\epsilon(t)$ after 9 weeks of accelerated testing. Here $(k, D_{d_1}, p, q, \alpha_1, r_1, r_2, \epsilon) = (5 \times 10^3, 3.5, 2, 0, 10^2, 1, 1, \frac{1}{8})$ and $\frac{\delta_\epsilon}{\delta_1} \ll 1$.

5.5 Summary and conclusions

5.5.1 Interpretations of the simulation results

1. The model shows several general characteristics one might expect:
   (a) Penetration-depth curves exhibit a near $t^{1/2}$-behavior for large t (cf. Fig. 8 , Fig. 13 - Fig. 16). Note: In the context of accelerated carbonation 6 to 9 weeks *is* large!
   (b) CO_2-curves correspond to results known from other models.
   (c) A large $Ca(OH)_2$-concentration gradient in Ω_2 near Ω_ϵ can be observed (cf. Fig. 7 (b)).
2. The model shows effects based on the two-zone- and moving-boundary setting:
   (a) The (example of) $Ca(OH)_2$-concentration profiles over several weeks (cf. Fig. 7 (b)) shows the effect of an accentuated ($\delta \gg 1$) influence of the reaction in Ω_ϵ. Although the model provides for an (indefinite) re-production of $Ca(OH)_2$ by dissolution, the consumption due to reaction (1) is much stronger than in Ω_1. This effect can be controlled quantitatively by the weighing parameter δ.
   (b) One of the motivation for the introducing a *two*-reaction-zones model has been the experimental observation, that after a fast increase of the carbonation degree near the front a slow (with respect to time) gradual increase occurs in Ω_1. This behavior of the model output is shown in Fig. 9 - Fig. 12, Fig. 17 and Fig. 18. A conjecture is, that the speed of this increase can be controlled by an appropriate (but not yet known) combination of δ_1 and δ_ϵ and the size of the reaction constant for the reaction on Ω_1.
   (c) The interplay between the two reaction zones is reflected by the (slight) increase of the $CaCO_3$ curve in the main-reaction zone Ω_ϵ if $\delta \gg 1$ (cf. Fig. 9 - Fig. 12). For $\delta \ll 1$ one obtains a slight decrease in Ω_ϵ (cf. Fig. 17 and Fig. 18).
3. A classification for the behavior of the penetration-depth curves with respect to p, q, r_1 and r_2 (cf. introduction of the reaction rates in (9), (12)) is open. In particular, one needs more information on which of these parameters are the more relevant ones. For a comprehensive model possibly modeling the carbonation of CSH-phases, too, an aproach using too many parameters will be useless due to the lack of data to fit these parameters.
   By a mere variation of p, q, r_1 and r_2, respectively, one obtains a large variety of carbonation-penetration depth curves and concentration profiles (cf. Fig. 8 , Fig. 13 - Fig. 16).

5.5.2 Conclusions

The two-reaction-zone model presented in this note shows several of the major characteristics expected from a carbonation-prediction model (shape of the curves, magnitude of the curves for real-material data). The model output is stable with respect to most of the parameters. The large variety of penetration-curves under a change of some of the

reaction-rates parameters indicates the necessity of a reduction of the number of reaction-rate parameters. Moreover, the introduction of two reaction zones (with possibly but not necessarily) different reaction rates allows a more detailed analysis of the carbonation behavior near and far from the reaction front and how this behavior can model-wise be controlled.

6 Appendix

Quantity	*Definition*	*Dimensions*	*Value/range*[a]
D_{w_1}, D_{w_2}	Effective moisture diffusivities, Refs. [46, 26]	$\text{cm}^2\ \text{day}^{-1}$	$[0.9, 90]$
D_{h_2}	Effective $Ca(OH)_2$(aq) diffusivity, Ref. [35]	$\text{cm}^2\ \text{day}^{-1}$	0.864
D_{c_1}	Effective CO_2(aq) diffusivity, Ref. [11]	$\text{cm}^2\ \text{day}^{-1}$	$[0.62, 6.2]$
$\lambda_{\bar{w}_i}$	Initial values of moisture $i = 1, 2$, Table 5	g cm^{-3}	$[0.061, 0.123]$
$\lambda_{\bar{d}}$	Initial concentration of CO_2(g), Ref. [45]	g cm^{-3}	58.92×10^{-4}
$\lambda_{\bar{b}}$	Initial value for $CaCO_3$	g cm^{-3}	0
$\lambda_{\bar{h}}$	Initial value for $Ca(OH)_2$(aq), Ref. [26]	g cm^{-3}	77.5×10^{-3}
s_0	Initial position cf. Fig. 6	cm	10^{-5}
$2L$	Length of the observed slab, Ref. [45]	cm	10
ϕ_1	Porosity of non-carbonated concrete, Ref. [26]	-	0.15
ϕ_2	Porosity of carbonated concrete, Ref. [26]	-	0.13
Q_H	Exchange term in Henry's law, Refs. [35, 6]	-	0.8227
P_H	Mass transfer coefficient of CO_2(g) in pore water, Ref. [6]	day^{-1}	35760
k_T	Mass transfer constant of CO_2(g), air to water, Ref. [6]	cm day^{-1}	7
$P_{\bar{h}kdiss}$	Factor in the dissolution law, $k = 1, \epsilon, 2$	day^{-1}	$\frac{1}{150}$
$\frac{A_s}{\phi_a}$	Surface area to volume ratio, for air, Ref. [6]	cm^{-1}	10^4
$\frac{A_s}{\phi_w}$	Surface area to volume ratio, for water, Ref. [6]	cm^{-1}	10^4

Table 1: Numerical data for several parameters and input variables.

[a]The threshold values introduced in this table are taken from the literature. We use numerical ranges and not precise values since we are not aware of measurements for these parameters within the ace in Ref. [45].

Quantity	*Definition*	*Dimensions*	*Value*
R	Gas constant, Ref. [13]	$\text{mol}^{-1}\ \text{K}^{-1}\ \text{atm}$	8206×10^{-5}
H	Henry's law constant for CO_2(g), Ref. [36]	$\text{mol m}^{-3}\text{atm}^{-1}$	34.2
M_{H_2O}	Molecular weight of water, Ref. [13]	g mol^{-1}	18
M_{CO_2}	Molecular weight of CO_2, Ref. [13]	g mol^{-1}	44
M_{CaCO_3}	Molecular weight of aragonite/calcite, Ref. [13]	g mol^{-1}	100.087
$M_{Ca(OH)_2}$	Molecular weight of $Ca(OH)_2$, Ref. [13]	g mol^{-1}	74
$\rho_{Ca(OH)_2}$	Density of $Ca(OH)_2$, Ref. [13]	g cm^{-3}	2.24
ρ_{CaCO_3}	Density of $CaCO_3$ (calcite), Ref. [13]	g cm^{-3}	2.71

Table 2: Useful physical and material constants.

Quantity	*Definition*	*Dimensions*	*Value*
w/c	Water:cement ratio	-	0.60
a/c	Aggregate:cement ratio	-	5.1429
ρ_c	Cement density, Refs. [45, 20]	g cm^{-3}	3.15
ρ_a	Aggregate density, Ref. [45]	g cm^{-3}	2.7
ρ_{H_2O}	Water density, Refs. [45, 20]	g cm^{-3}	1
ρ_{cp}	Cement paste density (CEM I 0.60), Ref. [45]	g cm^{-3}	1.7439
ρ_{CaO}	Calcium oxide density, Ref. [13]	g cm^{-3}	3.34

Table 3: Material characteristics of the concrete sample.

Portland cement (CEM I)	
SiO_2	20
Al_2O_3	6
Fe_2O_3	3
CaO	63
MgO	1.5
SO_3	2
Na_2O and K_2O	1
Others	1
Loss on ignition	2
Insoluble residue	0.5

Table 4: Composition (mass fraction %), cf. Ref. [27].

RH (%)	$\bar{w}$ (kg/m^3)
0	0
50	42
60	54
70	68
80	84
90	110
93	120
95	130

Table 5: Material data for concrete showing the relation between relative humidity RH and moisture content $\bar{w}$, cf. Ref. [1], III-4 . See also Fig. 4 in Ref. [22].

References

[1] J. Arfvidsson, Moisture transport in porous media. Modeling based on Kirchhoff potentials. Ph.D. Thesis, Lund Institute of Technology, 1998.

[2] P. W. Atkins, *Physical Chemistry.* Oxford University Press, Oxford, 1990.

[3] D. Bunte, *Zum karbonatisierungsbedingten Verlust der Dauerhaftigkeit von Auenbauteilen aus Stahlbeton* Ph.D. Thesis. Braunschweig, 1994.

[4] R. E. Beddoe, Private communications, (2002).

[5] M. Böhm, *Lecture Notes in Mathematical Modeling.* Bremen University, 2002.

[6] M. Böhm, J. Devinny, F. Jahani, G. Rosen, On a moving-boundary system modeling corrosion in sewer pipes. *Appl. Math. Comput.* **92**:247-269 (1998).

[7] M. Böhm, I. G. Rosen, Global weak solutions and uniqueness for a moving boundary problem for a coupled system of quasilinear diffusion-reaction equations arising as a model of chemical corrosion of concrete surfaces. Part 3, preprint, Humbold University, Berlin, 1997.

[8] M. Böhm, A. Muntean, Well-posedness of a reaction-layer model for predicting $Ca(OH)_2$ carbonation in concrete and a limit case. in preparation.

[9] M. Böhm, J. Kropp, A. Muntean, On a Prediction Model for Concrete Carbonation based on Moving Interfaces - Interface concentrated Reactions. *Berichte aus der Technomathematik*, University of Bremen, 2003. Submitted for publication.

[10] L. M. Brieger, F. H. Wittmann, Numerical simulation of concrete carbonation, in *Werkstoffwissenschaften und Bausanierung, Berichtstand zum 2. Int. Koll.* (F. H. Wittmann, Ed.), Technische Akademie Esslingen, 1986.

[11] T. Chaussadent, États des lieux et réflexions sur la carbonatation du béton armé. LCPC OA29, Laboratoire Central des Ponts et Chaussées, Paris, 1999.

[12] J. Crank, *Free and Moving Boundary Problems.* Clarendon Press, Oxford, 1984.

[13] *CRC Handbook of Chemistry and Physics.* (D. R. Lide, Ed.), CRC Press LLC, 2001-2002.

[14] Y. F. Houst, P. E. Roelfstra, F. H. Wittmann, A model to predict service life of concrete structures, in Werkstoffwissenschaften und Bausanierung. Berichtstand zum 2. Int. Koll. (F. H. Wittmann, Ed.), Technische Akademie Esslingen, 1986.

[15] L. Franke, K. Sisomphon, A new chemical method for analyzing free calcium hydroxide content in cementing material. submitted for publication, (2002).

[16] R. Gatignol, R. Prud'homme, *Mechanical and Thermodynamical Modeling of Fluid Interfaces.* World Scientific, Vol. 58, Singapore-New Jersey-London-Hong Kong, 2001.

[17] C. Gehlen, Lebensdauerbemessung- Zuverlassigkeitsberechnungen zur wirksamen Vermeidung von verschiedenartig induzierter Bewehrungskorrosion. *Beton-und Stahlbetonbau.* **7**:478-486 (2001).

[18] J. Grunewald *Documentation of the numerical simulation program DIM 3.1. Theoretical Fundamentals.* vol. 1, 2000.

[19] J. Grunewald, Mass and energy transport in porous media – Thermodynamical identification of driving potentials. *Internationale Zeitschrift für Bauinstandsetzen und Baudenkmalpflege.* **2**:113-142 (1999).

[20] R. Hohmann, M. J. Setzer, *Bauphysikalische Formeln und Tabellen.* Werner Verlag, Düsseldorf, 1995.

[21] Y. F. Houst, P. E. Roelfstra, F. H. Wittmann, A model to predict service life of concrete structures, in *Proc. Conf. Techn. Akademie Esslingen*, 1983.

[22] Y. F. Houst, The role of moisture in the carbonation of cementitious materials. *Internationale Zeitschrift für Bauinstandsetzen.* **2**:49-66 (1996).

[23] Y. F. Houst,F. H. Wittmann, Depth profiles of carbonates formed during natural carbonation. *Cem. Concr. Res.* **32**:1293-1930 (2002).

[24] T. Ishida, K. Maekawa, Modeling of pH profile in pore water based on mass transport and chemical equilibrium theory. *Concrete Library of JSCE.* **37**: 131-146 (2001).

[25] J. Kropp, Karbonatisierung und Transportvorgänge in Zementstein. Ph. D. Thesis, Karlsruhe, 1983.

[26] J. Kropp, Private communications, (2003).

[27] A. M. Neville, *Concrete Technology*. Pearson Higher Education, N.Y., 1994.

[28] M. Mainguy, Modèles de diffusion non-linéaires en milieux poreux. Application à la dissolution et au séchage des matériaux cimentaires. Ph. D. Thesis, École Nationale des Ponts et Chaussées, 1999.

[29] K. Maekawa, T. Ishida, Service-life evaluation of reinforced concrete under coupled forces and environmental actions, in *Transport in Cement-Based Materials, Materials Science of Concrete, Ion and Mass Transport*, The American Ceramic Society, 2000.

[30] J. Marchand, Modeling the behavior of unsaturated cement systems exposed to aggresive chemical environments. *Materials and Structures/Matériaux et Constructions*. **34**:195-200 (2001).

[31] A. M. Meirmanov, *The Stefan Problem*. De Gruyter Expositions in Mathematics, Berlin-New York, 1992.

[32] P. Moszkovicz, J. Pousin, F. Sanchez, Diffusion and dissolution in a reactive porous medium: Mathematical modeling and numerical simulations. *J. Comp. Appl. Math.* **66**:377-389 (1996).

[33] J. Ockendon, S. Howison, A. Lacey, A. Movchan, *Applied Partial Differential Equations*. Oxford University Press, Oxford, 1999.

[34] P. Ortoleva, G. Auchmuty, J. Chadam, J. Hettmer, E. Merino, C. H. Moore, Redox front propagation and banding modalities. *Physica D.* **19**:334-354 (1986).

[35] V. G. Papadakis, C. G. Vayenas, M. N. Fardis, A reaction engineering approach to the problem of concrete carbonation. *AIChE Journal.* **35**:1639-1650(1989).

[36] V. G. Papadakis, C. G. Vayenas, M. N. Fardis, Physical and chemical characteristics affecting the durability of concrete. *ACI Materials Journal.* **88**:186-196 (1991).

[37] V. G. Papadakis, C. G. Vayenas, M. N. Fardis, Fundamental modeling and experimental investigation of concrete carbonation. *ACI Materials Journal.* **88**:363-373 (1991).

[38] A. Pawell, K.-D. Krannich, Dissolution effects in transport in porous media. *SIAM J. Appl. Math.* **56**:89-118 (1996).

[39] J. Rubin, C. Wallis, Transport of reacting solutes subject to a moving dissolution boundary: Numerical methods and solutions. *Water Resources Research*, **23**:1231-1252 (1983).

[40] L. I. Rubinstein, *The Stefan Problem*. Transl. Math. Monographs, AMS, vol. 27, 1971.

[41] A. V. Saetta, B. A. Schrefler, R. V. Vitaliani, The carbonation of concrete and the mechanism of moisture, heat and carbon dioxide flow through porous materials. *Cem. Concr. Res.* **23**:761-772 (1993).

[42] A. V. Saetta, B. A. Schrefler, R. V. Vitaliani, 2-D model for carbonation and moisture/heat flow in porous materials. *Cem. Concr. Res.* **25**:1703-1712 (1995).

[43] E. Samson, J. Marchand, J. J. Beaudoin, Describing ion diffusion in cement-based materials using the homogenization technique. *Cem Concr. Res.* **29**:1341-1345 (1999).

[44] M. J. Setzer, U. Dahme, In preparation, 2003.

[45] K. Sisomphon, L. Franke, Private communications. (2003).

[46] A. Steffens, D. Dinkler, H. Ahrens, Modeling carbonation for corrosion risk prediction of concrete structures. *Cem. Concr. Res.* **32**:935-941 (2002).

[47] A. Steffens, Modellierung von Karbonatisierung und Chloridbindung zur numerischen Analyse der Korrosionsgefährdung der Betonbewehrung. PhD. Thesis, Technical University of Braunschweig, 2000.

[48] R. Temam, A. Miranville, *Mathematical Modeling in Continuum Mechanics*. Cambridge University Press, Cambridge, 2001.

Berichte aus der Technomathematik ISSN 1435-7968

http://www.math.uni-bremen.de/zetem/berichte.html

— Vertrieb durch den Autor —

Reports **Stand: 16. April 2003**

98–01. Peter Benner, Heike Faßbender:
An Implicitly Restarted Symplectic Lanczos Method for the Symplectic Eigenvalue Problem, Juli 1998.

98–02. Heike Faßbender:
Sliding Window Schemes for Discrete Least-Squares Approximation by Trigonometric Polynomials, Juli 1998.

98–03. Peter Benner, Maribel Castillo, Enrique S. Quintana-Ortí:
Parallel Partial Stabilizing Algorithms for Large Linear Control Systems, Juli 1998.

98–04. Peter Benner:
Computational Methods for Linear–Quadratic Optimization, August 1998.

98–05. Peter Benner, Ralph Byers, Enrique S. Quintana-Ortí, Gregorio Quintana-Ortí:
Solving Algebraic Riccati Equations on Parallel Computers Using Newton's Method with Exact Line Search, August 1998.

98–06. Lars Grüne, Fabian Wirth:
On the rate of convergence of infinite horizon discounted optimal value functions, November 1998.

98–07. Peter Benner, Volker Mehrmann, Hongguo Xu:
A Note on the Numerical Solution of Complex Hamiltonian and Skew-Hamiltonian Eigenvalue Problems, November 1998.

98–08. Eberhard Bänsch, Burkhard Höhn:
Numerical simulation of a silicon floating zone with a free capillary surface, Dezember 1998.

99–01. Heike Faßbender:
The Parameterized SR Algorithm for Symplectic (Butterfly) Matrices, Februar 1999.

99–02. Heike Faßbender:
Error Analysis of the symplectic Lanczos Method for the symplectic Eigenvalue Problem, März 1999.

99–03. Eberhard Bänsch, Alfred Schmidt:
Simulation of dendritic crystal growth with thermal convection, März 1999.

99–04. Eberhard Bänsch:
Finite element discretization of the Navier-Stokes equations with a free capillary surface, März 1999.

99–05. Peter Benner:
Mathematik in der Berufspraxis, Juli 1999.

99–06. Andrew D.B. Paice, Fabian R. Wirth:
Robustness of nonlinear systems and their domains of attraction, August 1999.

99–07. Peter Benner, Enrique S. Quintana-Ortí, Gregorio Quintana-Ortí:
Balanced Truncation Model Reduction of Large-Scale Dense Systems on Parallel Computers, September 1999.

99–08. Ronald Stöver:
Collocation methods for solving linear differential-algebraic boundary value problems, September 1999.

99–09. Huseyin Akcay:
Modelling with Orthonormal Basis Functions, September 1999.

99–10. Heike Faßbender, D. Steven Mackey, Niloufer Mackey:
Hamilton and Jacobi come full circle: Jacobi algorithms for structured Hamiltonian eigenproblems, Oktober 1999.

99–11. Peter Benner, Vincente Hernández, Antonio Pastor:
On the Kleinman Iteration for Nonstabilizable System, Oktober 1999.

99–12. Peter Benner, Heike Faßbender:
A Hybrid Method for the Numerical Solution of Discrete-Time Algebraic Riccati Equations, November 1999.

99–13. Peter Benner, Enrique S. Quintana-Ortí, Gregorio Quintana-Ortí:
Numerical Solution of Schur Stable Linear Matrix Equations on Multicomputers, November 1999.

99–14. Eberhard Bänsch, Karol Mikula:
Adaptivity in 3D Image Processing, Dezember 1999.

00–01. Peter Benner, Volker Mehrmann, Hongguo Xu:
Perturbation Analysis for the Eigenvalue Problem of a Formal Product of Matrices, Januar 2000.

00–02. Ziping Huang:
Finite Element Method for Mixed Problems with Penalty, Januar 2000.

00–03. Gianfrancesco Martinico:
Recursive mesh refinement in 3D, Februar 2000.

00–04. Eberhard Bänsch, Christoph Egbers, Oliver Meincke, Nicoleta Scurtu:
Taylor-Couette System with Asymmetric Boundary Conditions, Februar 2000.

00–05. Peter Benner:
Symplectic Balancing of Hamiltonian Matrices, Februar 2000.

00–06. Fabio Camilli, Lars Grüne, Fabian Wirth:
A regularization of Zubov's equation for robust domains of attraction, März 2000.

00–07. Michael Wolff, Eberhard Bänsch, Michael Böhm, Dominic Davis:
Modellierung der Abkühlung von Stahlbrammen, März 2000.

00–08. Stephan Dahlke, Peter Maaß, Gerd Teschke:
Interpolating Scaling Functions with Duals, April 2000.

00–09. Jochen Behrens, Fabian Wirth:
A globalization procedure for locally stabilizing controllers, Mai 2000.

00–10. Peter Maaß, Gerd Teschke, Werner Willmann, Günter Wollmann:
Detection and Classification of Material Attributes – A Practical Application of Wavelet Analysis, Mai 2000.

00–11. Stefan Boschert, Alfred Schmidt, Kunibert G. Siebert, Eberhard Bänsch, Klaus-Werner Benz, Gerhard Dziuk, Thomas Kaiser:
Simulation of Industrial Crystal Growth by the Vertical Bridgman Method, Mai 2000.

00–12. Volker Lehmann, Gerd Teschke:
Wavelet Based Methods for Improved Wind Profiler Signal Processing, Mai 2000.

00–13. Stephan Dahlke, Peter Maass:
A Note on Interpolating Scaling Functions, August 2000.

00–14. Ronny Ramlau, Rolf Clackdoyle, Frédéric Noo, Girish Bal:
Accurate Attenuation Correction in SPECT Imaging using Optimization of Bilinear Functions and Assuming an Unknown Spatially-Varying Attenuation Distribution, September 2000.

00–15. Peter Kunkel, Ronald Stöver:
Symmetric collocation methods for linear differential-algebraic boundary value problems, September 2000.

00–16. Fabian Wirth:
The generalized spectral radius and extremal norms, Oktober 2000.

00–17. Frank Stenger, Ahmad Reza Naghsh-Nilchi, Jenny Niebsch, Ronny Ramlau:
A unified approach to the approximate solution of PDE, November 2000.

00–18. Peter Benner, Enrique S. Quintana-Ortí, Gregorio Quintana-Ortí:
Parallel algorithms for model reduction of discrete–time systems, Dezember 2000.

00–19. Ronny Ramlau:
A steepest descent algorithm for the global minimization of Tikhonov–Phillips functional, Dezember 2000.

01–01. Efficient methods in hyperthermia treatment planning:
Torsten Köhler, Peter Maass, Peter Wust, Martin Seebass, Januar 2001.

01–02. Parallel Algorithms for LQ Optimal Control of Discrete-Time Periodic Linear Systems:
Peter Benner, Ralph Byers, Rafael Mayo, Enrique S. Quintana-Ortí, Vicente Hernández, Februar 2001.

01–03. Peter Benner, Enrique S. Quintana-Ortí, Gregorio Quintana-Ortí:
Efficient Numerical Algorithms for Balanced Stochastic Truncation, März 2001.

01–04. Peter Benner, Maribel Castillo, Enrique S. Quintana-Ortí:
Partial Stabilization of Large-Scale Discrete-Time Linear Control Systems, März 2001.

01–05. Stephan Dahlke:
Besov Regularity for Edge Singularities in Polyhedral Domains, Mai 2001.

01–06. Fabian Wirth:
A linearization principle for robustness with respect to time-varying perturbations, Mai 2001.

01–07. Stephan Dahlke, Wolfgang Dahmen, Karsten Urban:
Adaptive Wavelet Methods for Saddle Point Problems - Optimal Convergence Rates, Juli 2001.

01–08. Ronny Ramlau:
Morozov's Discrepancy Principle for Tikhonov regularization of nonlinear operators, Juli 2001.

01–09. Michael Wolff:
Einführung des Drucks für die instationären Stokes–Gleichungen mittels der Methode von Kaplan, Juli 2001.

01–10. Stephan Dahlke, Peter Maaß, Gerd Teschke:
Reconstruction of Reflectivity Desities by Wavelet Transforms, August 2001.

01–11. Stephan Dahlke:
Besov Regularity for the Neumann Problem, August 2001.

01–12. Bernard Haasdonk, Mario Ohlberger, Martin Rumpf, Alfred Schmidt, Kunibert G. Siebert:
h–p–Multiresolution Visualization of Adaptive Finite Element Simulations, Oktober 2001.

01–13. Stephan Dahlke, Gabriele Steidl, Gerd Teschke:
Coorbit Spaces and Banach Frames on Homogeneous Spaces with Applications to Analyzing Functions on Spheres, August 2001.

02–01. Michael Wolff, Michael Böhm:
Zur Modellierung der Thermoelasto-Plastizität mit Phasenumwandlungen bei Stählen sowie der Umwandlungsplastizität, Februar 2002.

02–02. Stephan Dahlke, Peter Maaß:
An Outline of Adaptive Wavelet Galerkin Methods for Tikhonov Regularization of Inverse Parabolic Problems, April 2002.

02–03. Alfred Schmidt:
A Multi-Mesh Finite Element Method for Phase Field Simulations, April 2002.

02–04. Sergey N. Dachkovski, Michael Böhm:
A Note on Finite Thermoplasticity with Phase Changes, Juli 2002.

02–05. Michael Wolff, Michael Böhm:
Phasenumwandlungen und Umwandlungsplastizität bei Stählen im Konzept der Thermoelasto-Plastizität, Juli 2002.

02–06. Gerd Teschke:
Construction of Generalized Uncertainty Principles and Wavelets in Anisotropic Sobolev Spaces, August 2002.

02–07. Ronny Ramlau:
TIGRA – an iterative algorithm for regularizing nonlinear ill–posed problems, August 2002.

02–08. Michael Lukaschewitsch, Peter Maaß, Michael Pidcock:
Tikhonov regularization for Electrical Impedance Tomography on unbounded domains, Oktober 2002.

02–09. Volker Dicken, Peter Maaß, Ingo Menz, Jenny Niebsch, Ronny Ramlau:
Inverse Unwuchtidentifikation an Flugtriebwerken mit Quetschöldämpfern, Oktober 2002.

02–10. Torsten Köhler, Peter Maaß, Jan Kalden:
Time-series forecasting for total volume data and charge back data, November 2002.

02–11. Angelika Bunse-Gerstner:
A Short Introduction to Iterative Methods for Large Linear Systems, November 2002.

02–12. Peter Kunkel, Volker Mehrmann, Ronald Stöver:
Symmetric Collocation for Unstructured Nonlinear Differential-Algebraic Equations of Arbitrary Index, November 2002.

02–13. Michael Wolff:
Ringvorlesung: Distortion Engineering 2
Kontinuumsmechanische Modellierung des Materialverhaltens von Stahl unter Berücksichtigung von Phasenumwandlungen, Dezember 2002.

02–14. Michael Böhm, Martin Hunkel, Alfred Schmidt, Michael Wolff:
Evaluation of various phase-transition models for 100Cr6 for application in commercial FEM programs, Dezember 2002.

03–01. Michael Wolff, Michael Böhm, Serguei Dachkovski:
Volumenanteile versus Massenanteile - der Dilatometerversuch aus der Sicht der Kontinuumsmechanik, Januar 2003.

03–02. Daniel Kessler, Ricardo H. Nochetto, Alfred Schmidt:
A posteriori error control for the Allen-Cahn Problem: circumventing Gronwall's inequality, März 2003.

03–03. Michael Böhm, Jörg Kropp, Adrian Muntean:
On a Prediction Model for Concrete Carbonation based on Moving Interfaces - Interface concentrated Reactions, April 2003.

03–04. Michael Böhm, Jörg Kropp, Adrian Muntean:
A Two-Reaction-Zones Moving-Interface Model for Predicting $Ca(OH)_2$ Carbonation in Concrete, April 2003.